Available online at www.sciencedirect.com

jmr&t Journal of Materials Research and Technology

journal homepage: www.elsevier.com/locate/jmrt

# Domination and effect of multi-parameters in direct chill casting based on establishment of thermo model by numerical simulation and experiment

*Jian Hou* [a], *Qichi Le* [a,*], *Liang Chen* [b], *Yonghui Jia* [c], *Chenglu Hu* [a], *Mohamed EI Amine Ben Seghier* [d]

[a] *Key Lab of Electromagnetic Processing of Materials, Ministry of Education, Northeastern University, Shenyang 110819, China*

[b] *Aero Engine Corporation of China Gas Turbine Co., Ltd., Shenyang 110167, China*

[c] *Key Laboratory for Light-weight Materials, Nanjing Tech University, No.5 Xin Mofan road, Nanjing 210009, China*

[d] *Department of Built Environment, Oslo Metropolitan University, Oslo, Norway*

ARTICLE INFO

*Article history:*
Received 23 June 2023
Accepted 23 September 2023
Available online 5 October 2023

*Keywords:*
DC casting
In-situ measurement
Thermo model
Magnesium alloys
Boiling heat transfer

ABSTRACT

In this paper, a mathematical model validated by in-situ temperature measurement data of the direct chill (DC) casting process has been established in order to study the domination and effect of multi-parameters including secondary cooling water flow rate (Q), casting speed (V), condition of primary cooling, and spraying water temperature ($T_w$) on DC casting index of sump depth ($d_{sump}$), maximum and minimum temperature gradient ($T_{g,max}$ and $T_{g,min}$) at mushy zone and shape of solidus line. Further, the height of impingement zone ($H_{ip}$) is systematic quantitative analysis by a novel designed test ($H_{ip} = 1.08865Q' + 0.06272V - 4.75597$). The calculated temperature using the numerical simulation exhibits a good match with the actual temperature measurement data. The results of multi-factors on index by the designed orthogonal test indicate that V dominates the $d_{sump}$ ($d_{sump} = 0.033 + 27.74V$) and $T_{g,min}$ ($T_{g,min} = 2569.15 - 766342.20V$) at mushy zone, Q dominates the $T_{g,max}$ ($T_{g,max} = 9195.12 + 2344770Q - 27.83T_w$) by analysing the range (R), variance (S) and significance (F). Likewise, by discussing the combination of R, S, F and microstructure observation, the priority influencing the shape of solidus line at center part was V. The Q dominates the shape of solidus line at the position between the center and edge part.



## 1. Introduction

Magnesium alloys offer the potential for weight and related energy savings in both the automotive and aerospace industries because they have the highest strength-to-weight ratio of common structural metals [1–7]. This potential advantage has recently driven an increased demand for cast and wrought magnesium products. With this increase, the direct chill (DC) casting process, which is used to produce the starting material for these applications, is receiving

* Corresponding author.
E-mail addresses: hj8111010@outlook.com (J. Hou), qichil@mail.neu.edu.cn (Q. Le), chensunlg@163.com (L. Chen), jiayh@njtech.edu.cn (Y. Jia), chengluhu1@163.com (C. Hu), moseg7662@oslomet.no (M.E. Amine Ben Seghier).

https://doi.org/10.1016/j.jmrt.2023.09.308

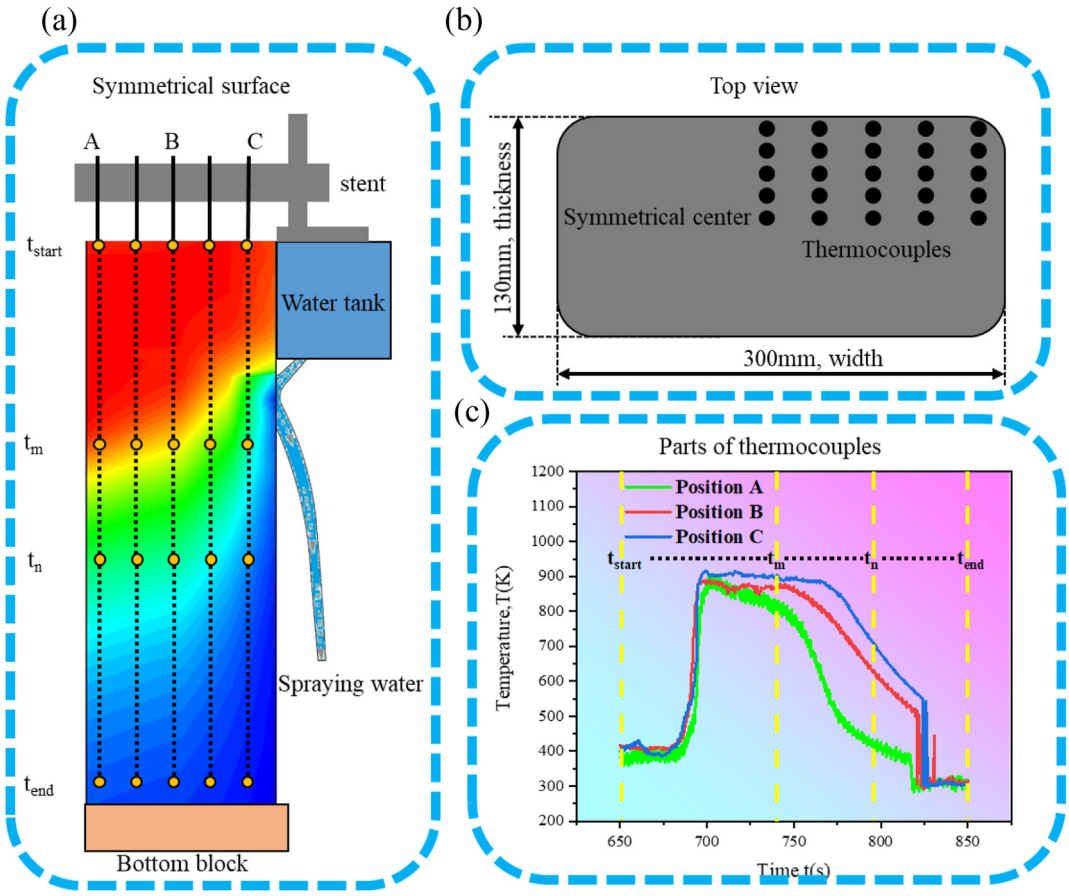


**Fig. 1 – Schematic illustration of temperature measurement during DC casting: (a) in-situ measurement of symmetrical surface on width direction; (b) location of thermocouples at top view; (c) temperature vs. time gained from thermocouples at position A, B and C.**

significantly more attention from the standpoint of process optimization [8–11].

Today's efforts concentrate on improving the quality control of the ingot. Over the last decade, the majority of research has used numerical modeling to enhance the existing process through a better understanding [12–15]. Due to the large number of processing parameters such as water flow rate, water temperature, casting speed, pouring temperature, grain refinement and casting parameters including sump depth, the shape of solidified shell, the thickness of mushy zone. The results in terms of ingot quality can vary greatly with even a slight change in casting parameters [16–21]. Furthermore, previous studies have shown that casting parameters such as water flow rate, water temperature, casting speed and pouring temperature have an impact on sump depth [22–26]. However, there has been insufficient discussion and analysis regarding which casting parameters dominate the variation of sump depth, temperature gradient of mushy zone and so on. This indicates that the industry's understanding of the process still needs improvement.

Among the numerous casting parameters, the status of cooling water plays an important role in heat transfer during the process of DC casting. Approximately 90 % of the total energy contained in the ingot is evacuated by water jet and free-falling water in the secondary cooling zone, while only 10 % is handled within the mold in the primary cooling zone [27–33]. Therefore, the cooling water is suspected to be a potential factor contributing to issues related to ingot quality.

Previous studies of secondary cooling in DC casting initially concentrated on the effects of processing parameters such as water flow rate, nozzle design, and cooling intensity [33–41]. The primary objective was to achieve a consistent cooling rate across the billet's cross-section, reduce thermal gradients, and promote desired microstructural characteristics [42–47]. These studies employed temperature measurement techniques and metallographic analysis to provide valuable insights into heat transfer mechanisms and the resulting microstructure [48–50].

Based on the statement above, in this paper, a systematic study on heat transfer of secondary cooling has been conducted including analyzing flow boiling mechanism of impingement zone and free-falling zone, developing the semi-empirical model of secondary cooling based on in-situ temperature measurement method and falling water film quenching test [19,29,42]. Further, the effect and domination of multi-parameters such as water flow rate of secondary cooling, casting speed, the status of primary cooling zone, temperature of water at secondary cooling zone on the index

of DC casting has been conducted by orthogonal method based on the verified model of secondary cooling zone.

## 2. Experiment

Undoubtedly, in-situ temperature measurement is a reliable method that provides valuable data for understanding the impact of secondary cooling on the temperature field during DC casting. However, this method is time-consuming and requires careful handling. Instrumenting thermocouples into the molten metal increases the risk for laboratory technicians. As a result, an alternative approach is proposed in this study, involving the use of a falling water film driven by gravity to quench preheated samples. This method allows for the simulation and discussion of the boiling mechanisms at impingement zone and free-falling zone, various factors influencing secondary cooling, such as the height of the impingement zone, water flow rate, and initial temperature of the slab surface.

### 2.1. *Melting and in-situ temperature measurement during DC casting and methods*

A schematic representation of a typical DC casting process and in-situ measurement is depicted in (Fig. 1(a)). The process involves the distribution of cooling water through a series of jets located at the bottom end of each casting mold [12–15]. When the liquid magnesium is poured into the mold, it comes into contact with the cooled surfaces of the mold and the bottom block, leading to the formation of a solidified shell through primary cooling. Heat transfer through conduction and convection subsequently transports the energy from the center of the ingot to the solidified shell. Inside the ingot, there is a temperature difference, creating a liquid magnesium pool known as the sump. The withdrawal speed of the ingot is gradually increased until it reaches a final constant value. Simultaneously, the temperature within the ingot changes over time. In the transient regime, the sump depth and the temperature distribution within the ingot approach their steady-state values.

The chemical composition of AZ80 alloy was shown in Table 1. The flammability of target melting alloys decreased due to the addition of element Y with the 1 % mass fraction. The liquidus and solidus temperatures of the final alloy were 879 K and 791 K respectively, determined by differential scanning calorimetry method [42]. The melting process for the preparation of the casting typically involved three steps. Firstly, the ingots of pure Mg and pure Al were melted together in an electrical resistance furnace. Secondly, the ingots of pure Zn, Mg–50%Y, and Mg–80%Mn master alloys were added to the melt at 973 K. Lastly, the temperature of the melt was maintained between 953 K and 973 K for 10 min after refinement and purification, before the casting process. A crystallizer made of aluminum was used in DC process to produce the AZ80 slab with a cross-section size of 300 mm × 130 mm.

**Table 1 – Chemical composition of AZ80-1Y (wt.%).**

| Al | Zn | Mn | Y | Mg |
|---|---|---|---|---|
| 8.0 | 0.7 | 0.48 | 1 | Bal. |

**Table 2 – Casting parameters of semi-continuous casting.**

| Experiment ($T_p$ = 923 K) | V mm/min | Q L/min | PC (insulation layer) | $T_w$ K |
|---|---|---|---|---|
| E1 | 80 | 40 | None | 293 |
| E2 | 80 | 70 | None | 293 |
| E3 | 120 | 40 | None | 293 |
| E4 | 80 | 40 | All surface | 313 |

The casting parameters of semi-continuous casting including secondary cooling water flow rate Q, pouring temperature $T_p$, casting speed V, the temperature of spraying water $T_w$ and status of insulation layer on inner face of mold PC shown in Table 2.

The continuous temperature measurement adopted in the present study is shown schematically in (Fig. 1(a)). The K-type thermocouples (chromel-alumel, with a single leg 0.2 mm in diameter) were fixed at various position by steel stent according to (Fig. 1(b)) and the temperature-measurement points were located above the crystallizer at first with a special distance to obtain the temperature variation with the real time or distance from the meniscus during the steady state of semi-continuous casting from beginning of the temperature-measurement points being driven downward into the melt by bottom block [20,42]. The temperature data obtained by HIOKI9334 logger communicator are presented as a function of time with 50 Hz acquisition rate or the distance to the top liquidus surface (by multiplying the casting velocity by casting time). As seen in (Fig. 1(c)), parts of thermocouples such as position A, position B and position C, the data of its temperature are captured at the $t_{start}$ at first and end with the time at $t_{end}$.

The specimens for microstructure observation were taken from the positions of the center to the edge along the width and thickness direction respectively.

### 2.2. *Falling water film quenching test on ingot produced by DC casting*

A comprehensive understanding of the heat exchange variation at the secondary cooling zone during DC casting relies heavily on accurately determining the surface heat flux density. To simulate the secondary cooling process during DC casting under controlled laboratory conditions, a series of carefully designed experiments were conducted. These experiments

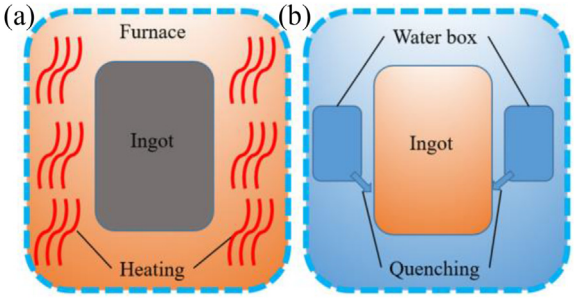


**Fig. 2 – Schematic diagram of DC secondary cooling simulator: (a) heating up to the target temperature; (b) cooling water quenching the ingot.**

involved the placement of thermocouples inside and around the samples to measure variations in sample surface temperature and the temperature of the surrounding environment (cooling water). The experimental steps, as seen in (Fig. 2 (a)) and (Fig. 2 (b)), including a raise-down device which can drive the ingot to move up and down and a water-spraying mold are developed to simulate the process of secondary cooling in our previous research [42]. The simulation of secondary cooling process is schematic illustrated in (Fig. 11 (a)). The detail of the simulation experiment is stated in section 3.5.3.

A series of K-type subsurface thermocouples are installed along thickness and width direction. The sample instrumented with thermocouples were heated up to the target temperature according to the water impingement points during the DC casting temperature-measurement before quenching. The water-spraying box produced jets of cooling water with a linear with flow rate density $\dot{Q}$, from 20 L/min · m to 100 L/min · m, and the surface temperature of ingot $T_i$ was also varied, ranging from 520 K to 670 K, to establish the relationship with the heat flux density.

In this study, the heat flux density is calculated using the inverse method to systematically examine the relationship between surface heat flux density and temperature. The temperature history, obtained from the subsurface thermocouple, and the thermophysical properties of AZ80, as shown in Fig. 4, are input into the inverse heat transfer calculation program to determine the surface heat transfer during the boiling process.

The whole process of inverse method is shown in Fig. 3, which can be classified into four main stage including preparation, setting initial conditions, calculating with several iterations and providing results [51]. The surface heat flux density is estimated from the initial temperature $T_i$ by minimizing the objective function shown in Eq (1):

$$F\left(h^{i}\right)=\frac{1}{M}\sum_{n=1}^{M}\left(T_{n}^{i+r\Delta\theta}-Y_{n}^{i+r\Delta\theta}\right)^{2} \tag{1}$$

Where $M$ is the number of the heat fluxes to be predicted, $T_n^{i+R\Delta\theta}$ and $Y_n^{i+R\Delta\theta}$ are the calculated and measured temperature at time $i+r\Delta\theta$, $r$ is the number of future time steps to compensate for the heat difference and $\Delta\theta$ is a discrete time interval. The objective function is minimized through iterations. At each iteration step, the heat flux density is increased by $\Delta h$. This procedure is continued until the ratio ($\Delta h/\ h$) becomes less than 0.001, and then an estimate of $h^i$ can be obtained. At this point, the time is increased by $\Delta\theta$, $qi$ is used as the initial heat flux guess for the next time step and the process is repeated for $h^{i+1}$, yielding the full history of q(t). Then, the interfacial heat flux density can be determined by the following Eq (2) [29]:

$$q=h(T_s-T_w) \tag{2}$$

### 2.3. Design of orthogonal experiment of DC casting with multi-factors $L_{16}(4^5)$

The math model of DC casting as can be seen in section 3.1 enables direct determination of the liquid cave depth, temperature gradient of the mushy zone, and curvature of the solidus line for different design parameters. However, due to the extensive computational requirements, this approach can be time-consuming and inefficient. To address this challenge, the orthogonal test method offers an efficient and systematic approach to evaluate the influence of various DC casting parameters. By conducting a limited number of numerical experiments, this method allows for the identification of preferred parameter values, leading to an optimal result [52–54].

The ranges and variation of the DC casting parameters, which are the factors of the array, are chosen according to a set of common and realistic specifications [55–58], which are Q (L/min), PC condition, V (mm/min), $T_w$ (K), Void (deviation data as an error reference). These five parameters are divided into four levels, the so-called narrow face which is the surface on thickness direction (130 mm) and the rolling face which is the surface on width direction (300 mm) as shown in Table 3, and an orthogonal test is carried out, using the orthogonal array $L_{16}(4^5)$, as shown in Table 4.

## 3. Modeling in DC casting

### 3.1. Numerical modelling

In current work, a three-dimensional mathematical model of AZ80 DC casting process is developed based on the continuum model by Bennon to compare and validate the semi-empirical models of secondary cooling and providing the dominance of the multi-factors influencing the casting indexes [58]. A consistent continuum approach is employed to solve the mass, momentum, and energy conservation equations for the solid-liquid phase change system. A single-region volume-averaged model is established, which applies the control equations to all regions of the solidification system, allowing computations to span the entire computational domain without the need for explicit delineation of solid, liquid, and mushy regions [59]. The following sections provide a detailed explanation of the numerical simulation control equations for the above-mentioned processes.

The mass conservation equation is shown in Eq (3):

$$\nabla\cdot\left(\rho_m\overrightarrow{V}\right)=0 \tag{3}$$

Where the $\rho_m$ is the density of melt during DC casting and the $\overrightarrow{V}$ is the speed vector.

The momentum conservation equation at x, y and z direction in a three-dimensional model is as follows:

$$\rho_m\left(\frac{\partial\overrightarrow{V_x}}{\partial t}+\overrightarrow{V_x}\frac{\partial\overrightarrow{V_x}}{\partial x}+\overrightarrow{V_y}\frac{\partial\overrightarrow{V_x}}{\partial y}+\overrightarrow{V_z}\frac{\partial\overrightarrow{V_x}}{\partial z}\right)=-\frac{\partial p}{\partial x}+\left(\mu_{lf}+\mu_{tf}\right)\left(\frac{\partial^2\overrightarrow{V_x}}{\partial x^2}+\frac{\partial^2\overrightarrow{V_x}}{\partial y^2}+\frac{\partial^2\overrightarrow{V_x}}{\partial z^2}\right)+\rho_m g\alpha\left(T-T_{ref}\right)+A_{mush}\frac{\left(1-f_l\right)^2}{f_l^3+\varphi}\overrightarrow{V_x} \tag{4}$$

$$\rho_m\left(\frac{\partial \overrightarrow{V_y}}{\partial t}+\overrightarrow{V_x}\frac{\partial \overrightarrow{V_y}}{\partial x}+\overrightarrow{V_y}\frac{\partial \overrightarrow{V_y}}{\partial y}+\overrightarrow{V_z}\frac{\partial \overrightarrow{V_y}}{\partial z}\right)=-\frac{\partial p}{\partial y}+\left(\mu_{lf}+\mu_{tf}\right)\left(\frac{\partial^2 \overrightarrow{V_y}}{\partial x^2}+\frac{\partial^2 \overrightarrow{V_y}}{\partial y^2}+\frac{\partial^2 \overrightarrow{V_y}}{\partial z^2}\right)+\rho_m g\alpha\left(T-T_{ref}\right)+A_{mush}\frac{\left(1-f_l\right)^2}{f_l^3+\varphi}\overrightarrow{V_y} \quad (5)$$

$$\rho_m\left(\frac{\partial \overrightarrow{V_z}}{\partial t}+\overrightarrow{V_x}\frac{\partial \overrightarrow{V_z}}{\partial x}+\overrightarrow{V_y}\frac{\partial \overrightarrow{V_z}}{\partial y}+\overrightarrow{V_z}\frac{\partial \overrightarrow{V_z}}{\partial z}\right)=-\frac{\partial p}{\partial z}+\left(\mu_{lf}+\mu_{tl}\right)\left(\frac{\partial^2 \overrightarrow{V_z}}{\partial x^2}+\frac{\partial^2 \overrightarrow{V_z}}{\partial y^2}+\frac{\partial^2 \overrightarrow{V_z}}{\partial z^2}\right)+\rho_m g\alpha\left(T-T_{ref}\right)+A_{mush}\frac{\left(1-f_l\right)^2}{f_l^3+\varphi}\left(\overrightarrow{V_z}-\overrightarrow{V_{cast}}\right) \quad (6)$$

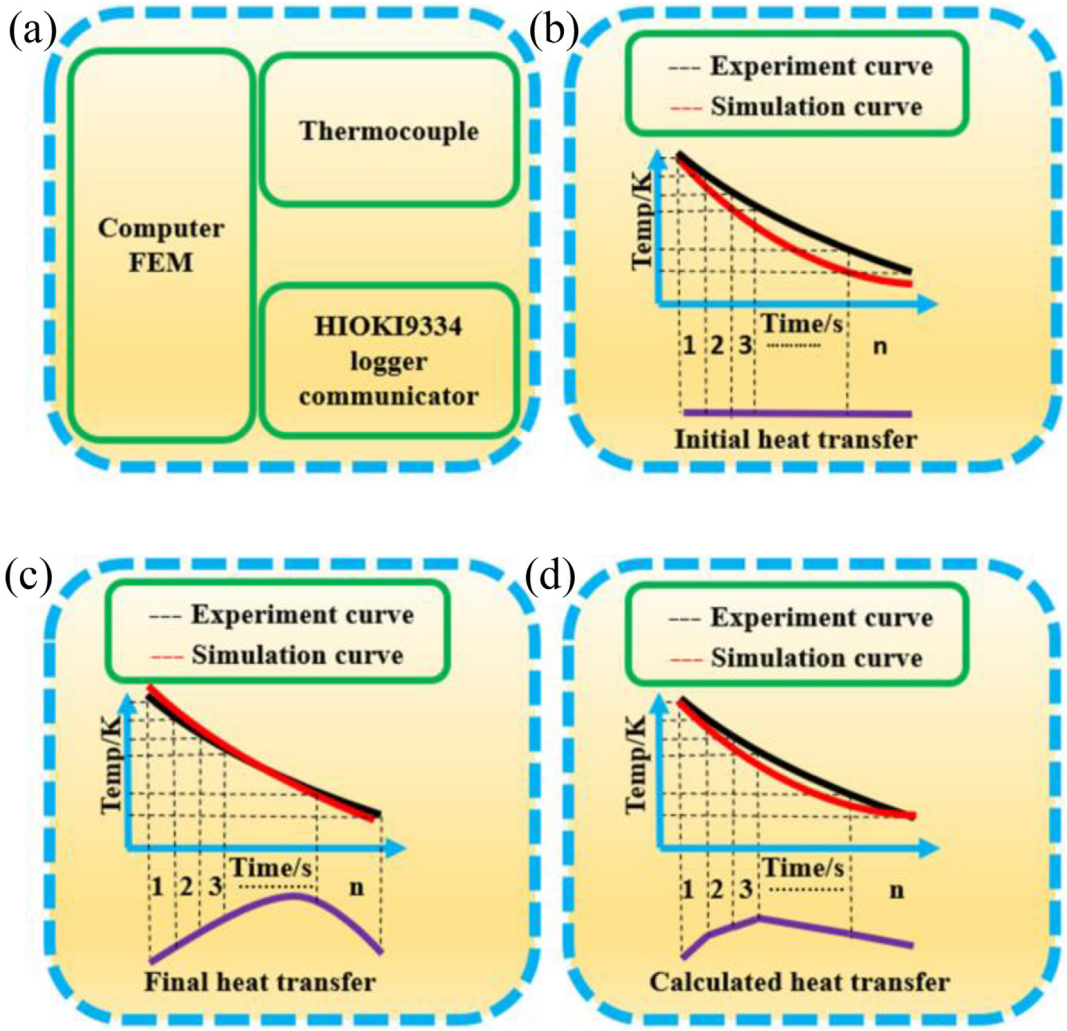


**Fig. 3 – Schematic diagram of reverse seeking process for heat transfer coefficient: (a) preparation before calculating; (b) setting the initial conditions; (c) calculating by several iterations; (d) final results by several iterations.**

In Eqs (4)–(6), the $\mu_{lf}$ and $\mu_{tl}$ represent the viscosities of laminar flow and turbulent flow. The $\overrightarrow{V_x}$, $\overrightarrow{V_y}$ and $\overrightarrow{V_z}$ represent the velocity components in the x, y and z directions, within a three-dimensional numerical model, respectively. Similarly, the $\overrightarrow{V_{cast}}$ denote the casting speed during DC casting. The $g$ and $\alpha$ correspond to gravity acceleration and coefficient of thermal expansion. The value of $\alpha$ is 2.7e-5 $K^{-1}$. Additionally, the $T$ and $T_{ref}$ represent the temperature of the ingot and the reference, respectively. The value of $T_{ref}$ is 835 K. The value of $\varphi$ is 1e-3, which is a small value to prevent the formula from being divided by zero, $A_{mush}$ is the mushy zone parameter, and the value is 1e5 kg/($m^3 \cdot s$).

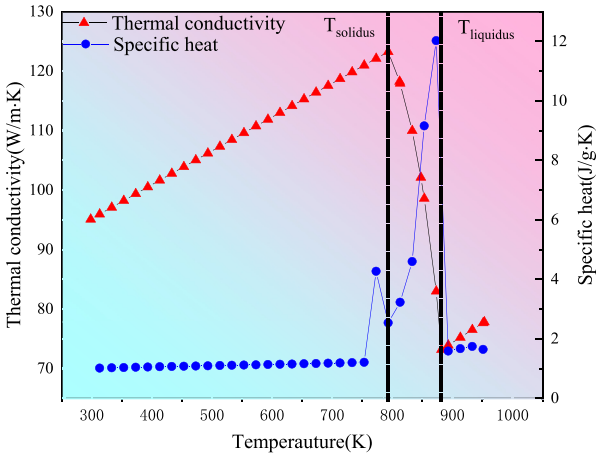


**Fig. 4 – Thermophysical properties of AZ80.**

**Table 3 – Factors and levels of DC casting parameters.**

| Levels | Q | PC (insulation layer) | V | $T_w$ | Void |
|---|---|---|---|---|---|
| 1 | 30 | All surface (PC1) | 60 | 283 | 1 |
| 2 | 50 | Narrow surface (PC2) | 80 | 293 | 2 |
| 3 | 70 | None (PC3) | 100 | 303 | 3 |
| 4 | 90 | Rolling surface (PC4) | 120 | 313 | 4 |

The energy conservation equation is shown in Eq (7):

$$\rho_m C_{p,eff}\frac{\partial T}{\partial t}+\rho_m C_{p,eff}\vec{V}\cdot\nabla T=\nabla\cdot(k\nabla T) \tag{7}$$

Where the $C_{p,eff}$ and $k$ represent the effective specific heat calculated by method of equivalent specific heat as shown in Eq (8). The relationship between $\beta_m$ and the fraction of solid and liquid phase is $\beta_m = (f_l - f_s)/2$. The thermophysical properties of AZ80 are shown in Fig. 4. In which the latent heat $L_{s,l}$ is taken into consideration by applying the equivalent specific heat method [20]. The value of $L_{s,l}$ is 309 kJ/kg.

**Table 4 – $L_{16}(4^5)$ orthogonal array testing for DC casting numerical simulation.**

| No. | Q | PC | V | $T_w$ | Void |
|---|---|---|---|---|---|
| 1 | 30 | PC1 | 60 | 283 | 1 |
| 2 | 30 | PC2 | 80 | 293 | 2 |
| 3 | 30 | PC3 | 100 | 303 | 3 |
| 4 | 30 | PC4 | 120 | 313 | 4 |
| 5 | 50 | PC1 | 60 | 293 | 4 |
| 6 | 50 | PC2 | 80 | 283 | 3 |
| 7 | 50 | PC3 | 100 | 313 | 2 |
| 8 | 50 | PC4 | 120 | 303 | 1 |
| 9 | 70 | PC1 | 60 | 303 | 2 |
| 10 | 70 | PC2 | 80 | 313 | 1 |
| 11 | 70 | PC3 | 100 | 283 | 4 |
| 12 | 70 | PC4 | 120 | 293 | 3 |
| 13 | 90 | PC1 | 60 | 313 | 3 |
| 14 | 90 | PC2 | 80 | 303 | 4 |
| 15 | 90 | PC3 | 100 | 293 | 1 |
| 16 | 90 | PC4 | 120 | 283 | 2 |

$$C_{p,eff}(T)=f_s\times C_{p,s}(T)+f_l(T)\times C_{p,l}(T)+L_{s,l}\frac{\partial(\beta_m)}{\partial T} \tag{8}$$

The lever rule is employed to calculate the liquid phase fraction $f_l$ and solid phase fraction $f_s$, with the equations shown in Eq (9) [9].

$$f_l=\begin{cases}0(if\ T<T_{solid})\\ \dfrac{T-T_{solid}}{T_{liquid}-T_{solid}}(\ if\ T_{solid}\le T\le T_{liquid})\\ 1(if\ T>T_{liuqid})\end{cases} \tag{9}$$

Where the $T_{liquid}$ and $T_{solid}$ denote the liquidus and solidus temperature of the alloy.

To accurately describe natural convection and forced convection in the DC casting process, it is essential to provide an accurate turbulence model during numerical simulations. In engineering applications, turbulence numerical simulations primarily include three methods: Direct Numerical Simulation (DNS), Large Eddy Simulation (LES), and solving the Reynolds-Averaged Navier-Stokes (RANS) equations. Among these methods, the RANS approach is widely used in solving engineering problems, including models such as the Reynolds stress model and the eddy viscosity closure model.

In the momentum equation, the turbulent viscosity, representing turbulent characteristics, is obtained from eddy viscosity theory, and it depends on the flow characteristics itself. In flow field calculations, the turbulent viscosity value is computed by augmenting the turbulence model equations. Turbulence models based on the eddy viscosity assumption include single-equation models, two-equation models, zero-equation models, and the low-Reynolds-number k-ε model, with the $k$-$\varepsilon$ two-equation model being a commonly used method.

In this paper, a semi-empirical standard $k$-$\varepsilon$ model is used, and the equations for turbulent kinetic energy $k$ and turbulent dissipation rate $\varepsilon$ are expressed as follows [18,49]:

$$\frac{\partial(\rho k)}{\partial t}+\rho_m\left(\vec{U}\cdot\nabla\right)k=\nabla\cdot\left[\left(\mu_{lf}+\frac{\mu_{tf}}{\sigma_k}\right)\nabla k\right]+p_k-\rho_m\varepsilon - A_{mush}\frac{(1-f_l)^2}{f_l^3+\varphi}k \tag{10}$$

$$\frac{\partial(\rho\varepsilon)}{\partial t}+\rho_m\left(\vec{U}\cdot\nabla\right)\varepsilon=\nabla\cdot\left[\left(\mu+\frac{\mu_t}{\sigma_\varepsilon}\right)\nabla\varepsilon\right]+c_a\frac{\varepsilon}{k}p_k-c_b\rho_m\frac{\varepsilon^2}{k} - A_{mush}\frac{(1-f_l)^2}{f_l^3+\varphi}\varepsilon \tag{11}$$

In Eq 10–13, the constants used in semi-empirical standard $k-\varepsilon$ model have the following values: $\sigma_k = 1.0$; $\sigma_\varepsilon = 1.3$; $c_a = 1.44$; $c_b = 1.92$; $c_\mu = 0.09$. The equations about $p_k$ and $\mu_{tf}$ are shown in Eq 12 and 13 as follows:

$$p_k=\mu_{tf}\left[\nabla\vec{V}:\left(\nabla\vec{V}+\left(\nabla\vec{V}\right)^{tf}\right)\right] \tag{12}$$

$$\mu_{tf}=\frac{\rho_m c_\mu k^2}{\varepsilon} \tag{13}$$

The equations above are solved by the software of Ansys Fluent. The detailed boundaries of fluid and thermal field are

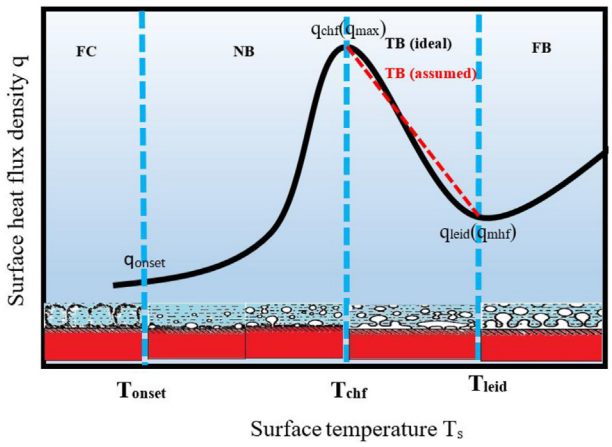


**Fig. 5 – Surface temperature $T_s$ vs. heat flux density $q$ of Leidenfrost boiling curve.**

given in section 3.4 and section 3.5. The temperature field results are given in section 5.

### 3.2. *Heat transfer boiling modelling of secondary cooling*

The heat flux density during secondary cooling is typically characterized by idealized boiling water curves. These curves are based on the well-known Leidenfrost boiling curve [61–65], which including four regimes: film boiling *FB*, transition boiling *TB*, nucleate boiling *NB*, and forced convection *FC* by surface temperature decreasing. These regimes are graphically illustrated in Fig. 5, presenting the relationship between the surface heat flux density and the surface temperature $T_s$. The temperature of minimum film boiling $T_{mhf}$ is similar to the temperature of Leidenfrost $T_{leid}$ [66,67]. The $T_{mhf}$ corresponds to the rewetting temperature for high mass flow rate bottom reflood. $T_{leid}$ is the rewetting temperature for droplet or sprays. The critical heat flux temperature, $T_{chf}$, is also called the temperature of maximum heat flux [61–63]. This temperature is the rewetting temperature for a falling film in top reflood.

During the *FB* stage, heat transfer occurs between the heated surface covered with a stable film and the surrounding vapor through conduction and convection. The Leidenfrost point $T_{leid}$ serves as the boundary between the *TB* stage and the *FB* stage. As for the *TB* stage, the heat exchange occurred between the heated surface covered with unstable film and part of the wetting region. The critical heat flux represents the upper limit of the boiling curve and delineates the boundary between the *NB* and *TB* intervals. For the *NB* stage, vapor bubbles are formed at the heated surface. Vapor structures vary from a few individual nucleation sites at low temperature to patches of coalesced bubbles and vapor columns as the heat flux density is increased. Below the onset of nucleate boiling pointed in Fig. 5, no vapor nucleation occurs, and the heat is removed by forced or natural convection.

In the case of DC casting, according to Fig. 6 film boiling can lead to the ejection of the water film away from the metal surface [29]. This phenomenon must be distinguished from the bounce-off of the water jet, which takes place in the impingement zone when the jet velocity $v_{jet}$ is too high or when the impingement angle is too large [40]. During the start-up stage and transition stage, as the ingot cooling progresses, the wetting zone increased, the temperature at the point of water ejection drops below the Leidenfrost point and the vapor film moves downward to regions where the surface temperature is higher [42,44]. The evolution of the rewetting front is illustrated in (Fig. 6 (a)) and (Fig. 6(b)). In steady-state, film boiling and water ejection do not occur, and the water film flows down the whole surface of the ingot. In consequence, the boiling occurred at the free-falling zone to follow the Leidenfrost boiling mechanism. While, due to the forced spraying water impinge on the surface, the NB dominate the impingement zone during the entire process of DC casting.

Based on the analysis above, four types including FB, TB, NB and convective cooling run through the whole secondary cooling process. The $T_{leid}$ and $T_{chf}$ are critical due to distinguishing the film boiling and nucleate boiling.

The film boiling dominate the whole process under the condition the surface temperature is higher than $T_{leid}$. The film boiling regime at free-falling zone can be modelled with two values: the minimum heat flux and the $T_{leid}$. As demonstrated

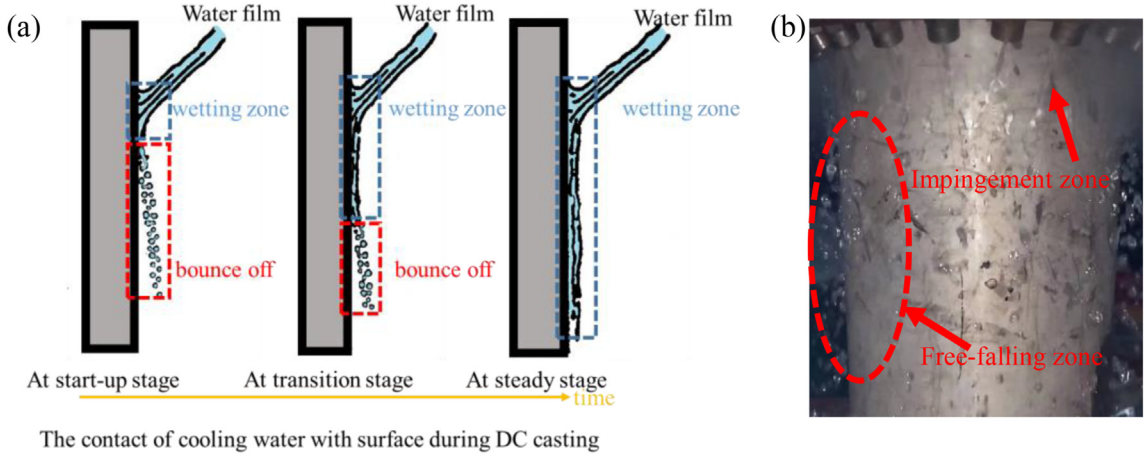


**Fig. 6 – Different boiling stage during DC casting (a) and Falling water quenching process at start-up stage in laboratory(b).**

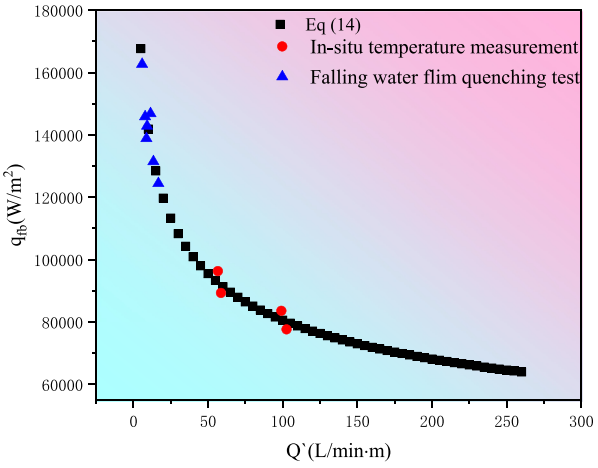


**Fig. 7 – Comparison between Eq (14) and experimental data of in-situ temperature measurement and falling water film quenching test.**

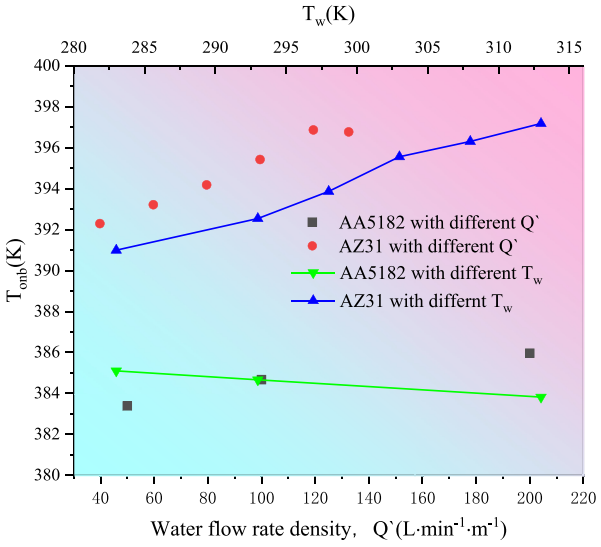


**Fig. 8 – The $T_{onb}$ at various Q` and $T_w$.**

by previous study [46,47,49], the heat flux is independent of the surface temperature in the film boiling regime. This heat flux is therefore equal to the minimal heat flux for any surface temperature above the Leidenfrost point. The Leidenfrost point temperature $T_{leid}$ represents the boundary between stable film boiling and transition boiling. Accurate knowledge of the Leidenfrost point is of critical importance when modelling the transient start-up phase of the DC casting process, because the heat flux is relatively low for stable film boiling, but increases significantly when transition boiling begins.

The average heat flux for film boiling is given by Eq (3). The Gravity number $G_n$ is equal to the Galilei number $P_e$ times the square of the Prandtl number Pr, and is given by the following Eq 14–20 [60]:

$$q_{fb,average} = \frac{2}{\sqrt{3\pi}} \frac{k_w}{L} \sqrt{\frac{\left(P_e^2 + 2G_n\right)^{\frac{3}{2}} - P_e^3}{G_n}} (T_{sat} - T_w) \tag{14}$$

$$\alpha = \frac{k_w}{\rho_w C_{p,w}} \tag{15}$$

$$\vartheta = \frac{\mu_w}{\rho_w} \tag{16}$$

**Table 5 – Thermophysical properties of cooling water.**

| Thermophysical properties | Parameter |
|---|---|
| Density, $\rho_w$ (kg/m$^3$) | 965.23 |
| Thermal conductivity, $k_w$ (W/ m·K) | 0.675 |
| Specific heat, $C_{p,w}$ (J/ kg·K) | 4205.54 |
| Viscosity, $\mu_w$ (kg/m·s) | 3.16E-04 |
| Saturation temperature, $T_{sat}$ (K) | 373.12 |
| Surface tension, $\sigma_w$ (N/m) | 0.059 |
| Latent heat, $L_w$ (K/kg) | 2257 |
| Prandtl number, $P_r$ | 1.97 |

$$Pr = \frac{\vartheta}{a_w} \tag{17}$$

$$P_e = \frac{v_0 L C_{p,w} \rho_w}{k_w} = \frac{v_0 L}{a_w} = \frac{v_0 H_{ip}}{a_w} \tag{18}$$

$$G_n = \frac{gL^3 C_{p,w}^2 \rho_w^2}{k_w^2} = \frac{gL^3}{a_w^2} = \frac{gH_{ip}^3}{a_w^2} = \frac{\rho_w g\, Pr^2 H_{ip}^3}{\mu_w^2} \tag{19}$$

$$v_0 = 0.0004524 Q` \sqrt{\frac{\rho_w g}{\mu_w}} \tag{20}$$

In which water film velocity $v_0$ is equal to the water flow rate in m$^3$/s · m divided by thethickness of the water layer in m. The thickness of a free-falling water film is itself a function of the water flow rate density Q`, the density $\rho_w$ and the viscosity $\mu_w$.

The length L corresponds to the height of the impingement zone $H_{ip}$ which is particularly important during the whole process of DC casting, due to its higher cooling intensity.

As can be seen in Fig. 7, the experimental data shows a high degree of fit with the model of Eq (14). In consequence, the model of Eq (14) is applicable for film boiling in this paper.

During the nucleate boiling stage, various models have been proposed to describe the heat flux, most of which fall under the category of the superposition approach. This approach, introduced by Chen [68], assumes that the total wall heat flux can be linearly decomposed into a convective component and a nucleate boiling component, as shown in Eq (21). This linear decomposition is appealing for two main reasons. Firstly, it allows for flexibility in selecting the most appropriate submodels for each component. Secondly, it ensures the correct asymptotic behavior as the system transitions to the non-boiling regime. Specifically, when the surface temperature $T_s$ is lower than the onset nucleation temperature $T_{onb}$, the nucleate boiling component $q_{nb}$ becomes zero, and only the macroscopic, single-phase convection component ($q_c$) remains.

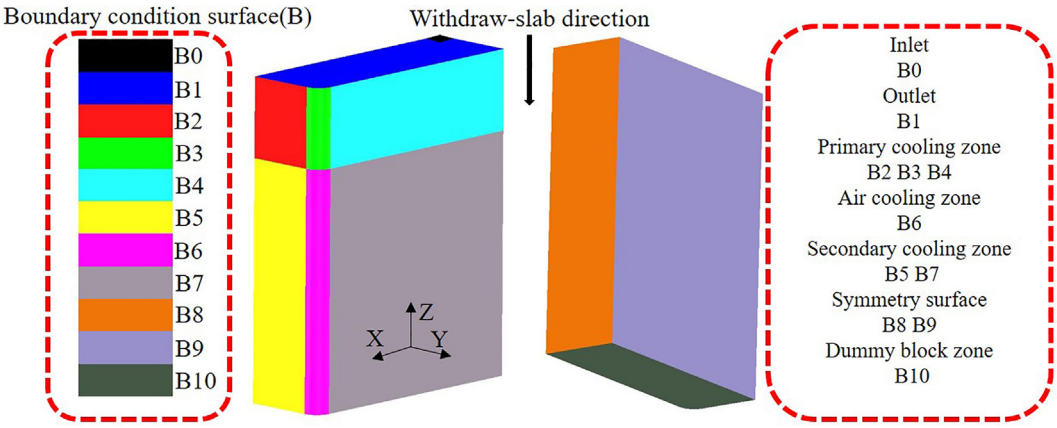


**Fig. 9 – Description of fluid and temperature field boundary conditions.**

$$q_{total} = q_{nb} + q_c \tag{21}$$

In nucleate boiling component, the heat flux of nucleate boiling $q_{nb}$ modelled by Rohsenow [69,70] was found to be a function of several parameters including water thermophysical properties, solid surface roughness and so on, as described in Eq (22):

$$\frac{C_{p,l}\Delta T}{L_{lg}} = C_{sf}\left[\frac{q_{nb}}{L_{lg}\mu_l}\sqrt{\frac{\sigma_l}{g(\rho_l-\rho_g)}}\right]^{c1}\left(\frac{C_{p,l}\mu_l}{k_f}\right)^{c2} \tag{22}$$

Furthermore, according to Rohsenow [69–72], whereas $c1$ is not affected, $c2$ might depend upon the surface finishing, attaining values in the range between 0.8 and 2.0. Because the different thermophysical properties of water at its saturation temperature are constant, the heat flux for nucleate pool boiling can be simplified to:

$$q_{nb} = C_b\Delta T_{sat}{}^{c3} = C_b(T_s - T_{sat})^{c3} \tag{23}$$

In convective component, the heat flux of convective $h_c$ for a free-falling film of water in Eq 24 and 25 obtained from many researchers which can be generalized in Eq (26):

$$Nu = CRe^i\, Pr^j Gn^{0.33} \tag{24}$$

**Table 6 – Fluid field boundary conditions.**

| Boundaries | Fluid boundary conditions |
|---|---|
| Inlet (B0) | $V_{inlet} = V_z = \frac{V_{cast}}{S_{inlet}+S_{outlet}}$ <br> $k_{ke} = 0.01 \times V_{cast}^2\ \varepsilon_{dr} = \frac{k_{ke}^{1.5}}{R_{inlet}}$ |
| Outlet (B1) | $V_x = 0\ V_y = 0\ V_z = 0$ |
| Primary cooling zone (B2, B3, B4) | $V_x = 0\ V_y = 0\ V_z = 0$ |
| Air cooling zone (B6) | $V_x = 0\ V_y = 0\ V_z = V_{cast}$ |
| Secondary cooling zone (B5, B7) | $V_x = 0\ V_y = 0\ V_z = V_{cast}$ |
| Surface of symmetry (B8, B9) | $V_x = 0\ V_y = 0\ V_z = 0$ |
| Bottom block zone (B10) | $V_x = 0\ V_y = 0\ V_z = V_{cast}$ |

$$h_c = \frac{Nuk_f}{L} \tag{25}$$

$$h_c = C\frac{k_f}{L}Re^i\, Pr^{0.4}Gn^{0.33} \tag{26}$$

It has been well established in previous investigations that the Prandtl number dependence approximately follows a $Nu \propto Pr^{0.4}$ relationship [72]. Choosing this as the appropriate Prandtl number dependence, several functions were evaluated, and the following expression provided an uncomplicated relationship that proved sufficiently accurate.

In transient boiling conditions, the transition boiling regime plays a crucial role as an intermediate state between film boiling and nucleate boiling. During this regime, as the surface temperature decreases, the wetted area of the surface covered by the cooling water increases, while the portion covered by the vapor blanket decreases.

To overcome the lacking mathematical models for the transition boiling stage, previous studies have made certain

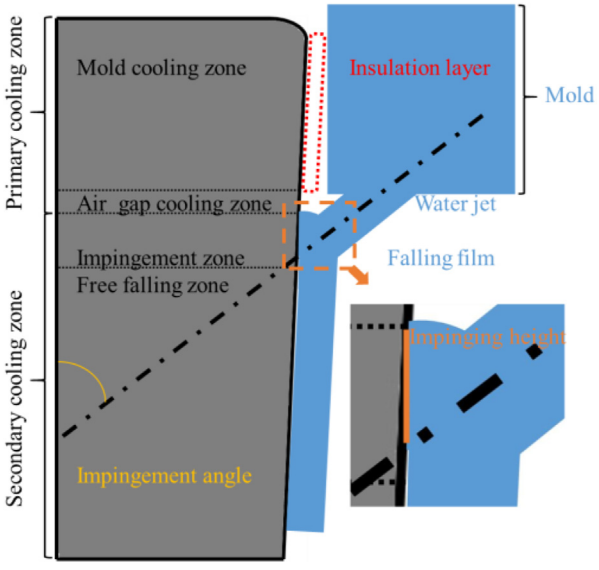


**Fig. 10 – Schematic illustration of primary cooling zone and secondary cooling zone.**

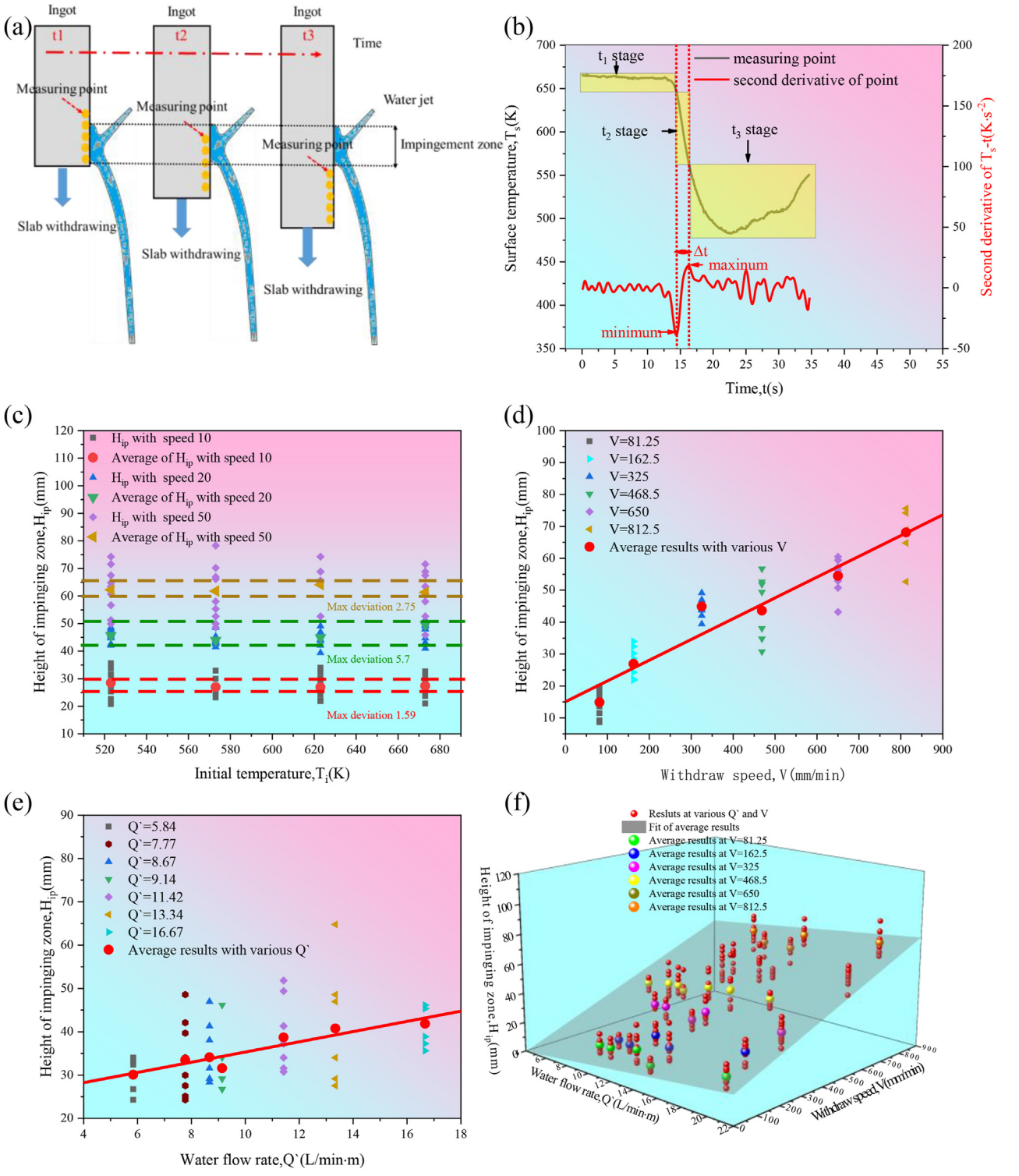


**Fig. 11 – Schematic illustration of calculating $H_{ip}$ (a, b) and parameters (c, initial temperature of ingot), (d, casting speed), (e, spraying water flow rate density) effect on $H_{ip}$.**

assumptions [68–74]. One common assumption is that the slope of the boiling curve ($q$-$T_s$) remains constant throughout the transition regime, as illustrated in Fig. 5. The heat flux during the transition boiling stage can be described using a specific equation seen in Eq (27), which considers the contributions from both films boiling and nucleate boiling:

$$q_{tb} = \frac{T_{leid} - T_s}{T_{leid} - T_{chf}}\left(q_{chf} + q_c\right) + \frac{T_s - T_{chf}}{T_{leid} - T_{chf}} q_{fb} \quad \left(T_{chf} < T_s < T_{leid}\right) \tag{27}$$

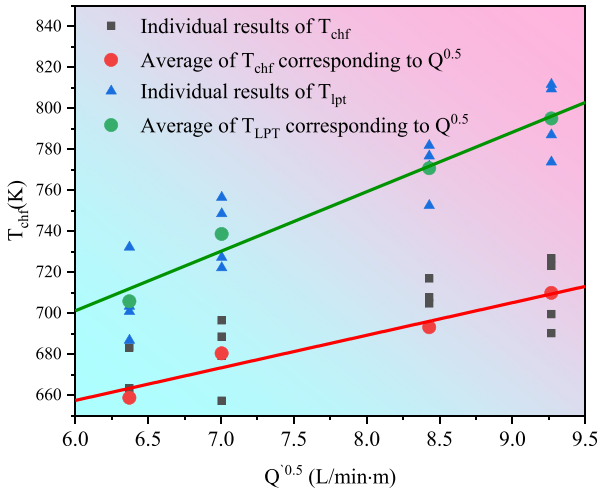


**Fig. 12 – The relationship between $T_{leid}$, $T_{chf}$ and the square root of secondary cooling water flow rate per unit of perimeter.**

### 3.3. *Assumptions and simplification of mathematic model*

There are some assumptions need to be made in this model:

1) The meniscus surface is assumed to be flat, and the calculation of the solute field is not included in this model;
2) The fluid is incompressible;
3) When the value of wall temperature is below 373 K, the heat transfer coefficient considered to be constant;
4) The thermophysical properties of cooling water are constant, as can be seen in Table 5 [75];
5) Due to the problem of lacking mathematical models in transition boiling stage, the boiling curve of $q$-$T_s$ in transition regime was assumed to be constant as mentioned in section 3.2;
6) The largest displacement was assumed to occur at the edges of the ingot during heat transfer of the bottom block zone, and no displacement was assumed to occur at the zone of $h_{contact}$, as seen in Fig. 14. Moreover, the cooling water was assumed to wet the butt curl, which means there are none interaction between water and ingot at center part. The heat transfer at wetted part was simplified to match the heat transfer at free-falling zone;
7) As depicted in Fig. 8, previous research on aluminum alloys as well as the current study on AZ80 reveals that the $T_{onb}$ remains largely unaffected by variations in Q and $T_i$ [38]. Based on this observation, it is reasonable to assume in this paper that $T_{onb}$ remains constant throughout the analysis. To ensure a representative value, the average of $T_{onb}$ from numerous experimental results is applied.

### 3.4. *Fluid field boundary condition*

The fluid field boundary condition during the whole numerical calculation should be classified into several parts refer to Fig. 9 and Table 6. The $k_{ke}$ and $\varepsilon_{dr}$ represent the turbulent energy and turbulent dissipation rate. The $S_{inlet}$ and $S_{outlet}$ represent the area of inlet and outlet.

### 3.5. *Thermal condition*

#### 3.5.1. *Inlet and outlet zone and symmetry surface*

The temperature of inlet B0 is constant value and equals to pouring temperature. Air cooling dominate the outlet zone B1 with a constant heat transfer coefficient value is 200 $W/m^2 \cdot K$. Heat loss along the symmetry surface boundary B8 and B9 is considered to be zero due to the axis of symmetry.

#### 3.5.2. *Primary cooling zone*

In primary cooling zone B2, B3 and B4, about 10 % of the total heat during DC casting is extracted from the melting in crystallizer [27]. The value of the heat transfer at primary cooling zone dominate the initial temperature of solidified surface and its quality, moreover, subsequently influencing the boiling water heat transfer below the primary cooling zone.

Fundamental and systematic work has been done by several researchers on heat transfer behavior of mold cooling during casting process [29,36,38,40,44]. The general character is found in the mold cooling which can be typically classified into two stage shown in Fig. 10: (a) at first stage, the melting directly contacts with the crystallizer inner wall cooled by the flowing water, which exhibits extremely heat transfer

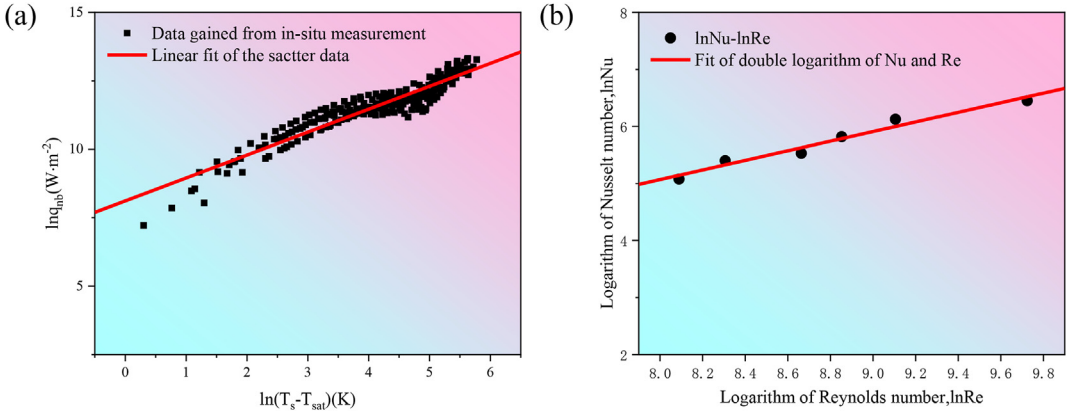


**Fig. 13 – The quantitative analysis of $q_{nb}$ and $q_c$: (a) $lnq_{nb}$ vs. ln ($T_s$-$T_{sat}$); (b) *lnNu* vs. *lnRe*.**

**Table 7 – Variations of primary cooling zone heat transfer coefficient $h_{pc}$ as a function of the billet surface temperature $T_s$**

| Billet surface temperature, $T_s$ (K) | Heat transfer coefficient, $h_{pc}$ (W/m$^2$·K) |
|---|---|
| $T_s \geq 863$ | 1500 |
| $833 \leq T_s < 863$ | $47.5T - 39492.5$ |
| $803 \leq T_s < 833$ | 75 |
| $783 \leq T_s < 803$ | $2.5T - 1932.5$ |
| $T_s < 783$ | 25 |

coefficient and possesses less than 90 % of total heat in primary cooling zone; (b) at last stage, air gap formed between the solidified metal and mold inner wall due to volumetric shrinkage of the solidifying metal, which exhibits extremely lower heat transfer coefficient compared to first stage due to air cooling.

To describe these effects, the heat transfer coefficient $h_{pc}$ at the billet/mold interface has been formulated to vary as a function of the local surface temperature as shown in Table 7 [42,46,49].

### 3.5.3. *Secondary cooling zone*

Secondary cooling refers to the area below the mold contacting with water and can be divided into an impingement zone and a free-falling zone as shown in Fig. 10. The impingement zone can be further subdivided into the two regions below and above the impingement point [47]: the zone below impingement point exhibits relatively higher heat transfer coefficient compared to the upper zone, the upper impingement zone corresponds to a region of back flow which is also called climb height. According to Fig. 10, the location of climb height corresponds to the impingement angle, the climb height moving upward with the increasing impingement angle. To avoid the direct contact between the cooling water and melting, the impingement angle of the water jets is typically in the range 15–30° [38].

The height of the impingement zone $H_{ip}$ depends on a number of factors such as the cooling Q, V, surface condition and so on. The $H_{ip}$ can be attributed to a wide range of values between 5 mm and 300 mm [29]. It is therefore critical, when modelling the direct-chill casting process, to know the height of the impingement zone $H_{ip}$. This is particularly important during the transient start-up phase of the process, because high temperature phenomena such as stable film boiling can only take place in the impingement zone, whereas water film ejection can only occur in the free-falling zone.

**Table 8 – The total heat flux density at free-falling zone.**

| Surface temperature | Boiling mechanism | Total heat flux density |
|---|---|---|
| $T_s \geq T_{leid}$ | Film boiling | $q_{total} = q_{fb}$ |
| $T_{chf} < T_s < T_{leid}$ | Transition boiling | $q_{total} = q_{tb} = \frac{T_{leid} - T_s}{T_{leid} - T_{chf}}(q_c + q_{chf}) + \frac{T_s - T_{chf}}{T_{lpt} - T_{chf}} q_{fb}$ |
| $T_{onset} < T_s < T_{chf}$ | Nucleate boiling | $q_{total} = q_{nb} + q_c$ |
| $T_s \leq T_{onset}$ | Convective cooling | $q_{total} = 200(\mathrm{W/m^2})$ |

The falling water film quenching tests with a moving ingot also called rewetting test, which serve as a valuable method for quantifying the $H_{ip}$. These tests involve conducting experiments with a moving sample and initially high temperature. In the initial phase of the test, the rapid ejection of the free-falling water film results in cooling primarily within the impingement zone. An example of the temperature history recorded during a rewetting test is shown in (Fig. 11(b)).

During the test, the first set of thermocouples captures a noticeable temperature drop as the cooling water jets contact the bottom surface of the instrumented sample. As the sample is gradually lowered, the impingement point moves up along the surface, leading to the ejection of the water film into the free-falling zone. At this stage, the surface undergoes cooling predominantly through natural air convection, which causes heat to flow back to the surface and results in reheating.

As depicted in (Fig. 11(a)) and (Fig. 11(b)), the entire process can be categorized into three stages based on the progression of time:(a) At t1 stage, the free-falling water film reaches the measuring point, leading to a decrease in temperature at the measuring point. This temperature decrease can be attributed to the advanced cooling front effect and the influence of air convection; (b) At t2 stage, the measuring point becomes fully covered by the jetting water film. During this stage, there is a sharp temperature decrease due to the unique and highly intensified impinging and wetting effects within the impingement zone; (c) At t3 stage, the free-falling water film moves upward relative to the measuring point, and the measuring point is now located in the ejecting zone. In this stage, the heat transfer through stable film boiling is relatively low, resulting in a phenomenon of reheating with an increase in temperature at the measuring point.

The (Fig. 11(b)) exhibits a curve of the second derivative of temperature with respect to time for a subsurface thermocouple. Despite the significant amount of signal noise, the minimum and maximum of second derivative of $T_s$ (K/s$^2$) as marked in (Fig. 11(b)) are easy to identify.

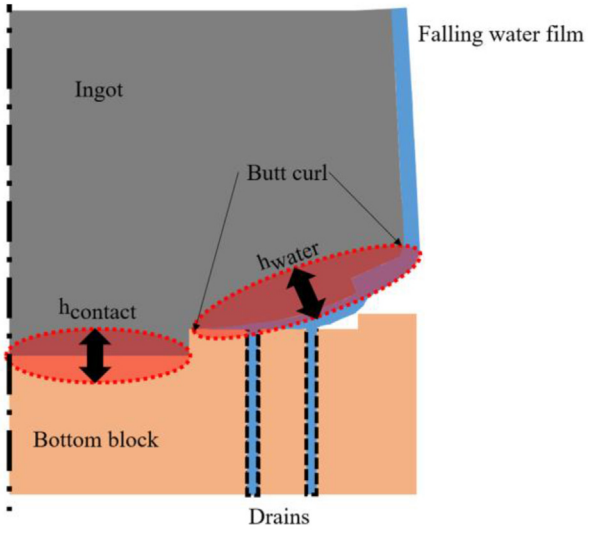


**Fig. 14 – Schematic illustration of heat transfer at bottom block zone.**

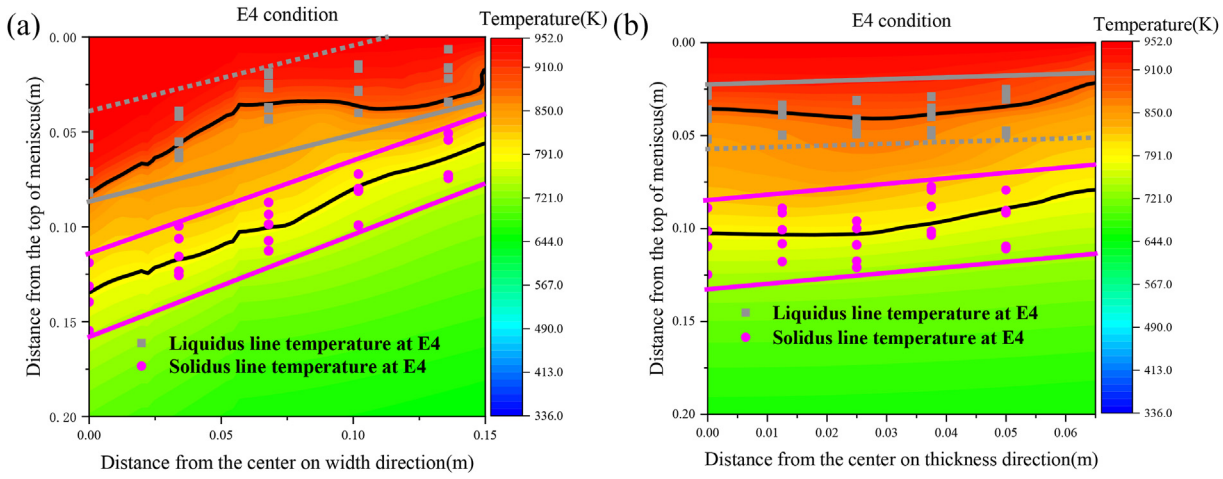


**Fig. 15 – Comparisons of results between the numerical simulation and in-situ temperature measurement: (a) width direction; (b) thickness direction.**

The $H_{ip}$ could be calculated by dividing the time interval between the minimum and the maximum by the sample moving speed in Eq (28):

$$H_{ip} = \frac{\Delta t}{V} \tag{28}$$

The $H_{ip}$ was measured for various factors including water flow rate density Q‘ (L/min · m), withdraw speed (casting speed V, mm/min) and initial temperature $T_i$ (K) shown in (Fig. 11(c)), (Fig. 11(d)), (Fig. 11(e)) and (Fig. 11(f)). The effect of initial temperature on $H_{ip}$ can be neglected according to (Fig. 11(c)). Additionally, both V and Q′ exhibit a positive linear relationship with $H_{ip}$ as can be seen in (Fig. 11(d)) and (Fig. 11(e)), which correlation coefficient of are 0.95 and 0.94 respectively. Based on the analysis above, establishing the relationship among the $H_{ip}$, V and Q′ is necessary. According to (Fig. 11(f)), the expression is given as follows:

$$H_{ip} = 1.08865Q' + 0.06272V - 4.75597, R^2 = 0.95 \tag{29}$$

**Table 9 – Index of sump depth ($d_{smup}$), the maximum and minimum of temperature ($T_{g,min}$, $T_{g,max}$) at mushy zone designed on orthogonal test.**

| No. | $d_{smup}$ (mm) | $T_{g,min}$ (K/m) | $T_{g,max}$ (K/m) |
|---|---|---|---|
| 1 | 58.4 | 1901.22 | 2725.35 |
| 2 | 66.98 | 1604.53 | 2441.34 |
| 3 | 79.7 | 1332.23 | 2318.85 |
| 4 | 98.2 | 831.81 | 1992.74 |
| 5 | 68.9 | 1511.93 | 2658.82 |
| 6 | 60.8 | 1858.47 | 2447.79 |
| 7 | 91.6 | 934.38 | 3195.49 |
| 8 | 76.4 | 1384.44 | 2459.66 |
| 9 | 72.5 | 1413.67 | 3303.65 |
| 10 | 88.84 | 1017.99 | 3512.83 |
| 11 | 62.8 | 1751.95 | 3872.04 |
| 12 | 72.55 | 1411.81 | 3792.74 |
| 13 | 83.17 | 1158.91 | 4925.51 |
| 14 | 73.16 | 1378.71 | 5516.09 |
| 15 | 67.6 | 1572.04 | 4217.48 |
| 16 | 65.11 | 1650.14 | 4000.56 |

As it is known to all, there are several factors influencing the $T_{leid}$ and $T_{chf}$ such as pressure, subcooling, surface conditions, material properties, flow rate and the composition of liquid. A series of tests conducted on aluminum AA5182 samples provided a relationship between the $T_{leid}$ and Q′ in Eq (30) [34,38]. The Leidenfrost temperature is sensitive to Q‘:

$$T_{leid,AA5182} = 373 + 33.0\sqrt{Q'} \tag{30}$$

Consequently, in this paper, assumptions and simplifications are given as flow rate dominate the $T_{chf}$ and $T_{leid}$ during secondary cooling process in numerical calculation on thermal condition. The relationship between $T_{leid}$, $T_{chf}$ and Q based on in-situ experiment are shown in Fig. 12. The average $T_{leid}$, average $T_{chf}$ and $\sqrt{Q'}$ exhibit a positive quasi-linear relationship as shown in Eq (31) and Eq (32) respectively:

$$T_{leid,average} = 29.06\sqrt{Q'} + 526.81, R^2 = 0.98 \tag{31}$$

$$T_{chf,average} = 15.90\sqrt{Q'} + 561.99, R^2 = 0.96 \tag{32}$$

The transition from laminar to turbulent film flow occurs when the Reynolds number exceeds 2000. The Reynolds number *Re* is defined by Eq (33):

$$Re = \frac{\rho_w v_w dn}{\mu_w} = \frac{\rho_w Q}{\pi dn \mu_w} \approx \frac{1.6\rho_w Q}{L_c \mu_w} = \frac{1.6\rho_w Q'}{\mu_w} \tag{33}$$

Where $L_c$ is the sum length of four straight, as seen in (Fig. 1(b)).

Based on section 3.2 and double logarithmic graph gained from the data of in-situ temperature measurement as seen in (Fig. 13(b)), an intuitive understanding on lnNu number exhibiting a positive linear regression on lnRe, Eq 34 and 35 is shown as follows:

$$lnNu = 0.84lnRe + 0.4lnPr + 0.33lnGn - 2.53, R^2 = 0.97 \tag{34}$$

$$Nu = 0.08Re^{0.84}\, Pr^{0.4} Gn^{0.33} \tag{35}$$

Combined with Eq 15–17, Eq (19), Eq 24–26 and Eq 33–35. As a result, the $q_c$ can be expressed as follows in Eq (36):

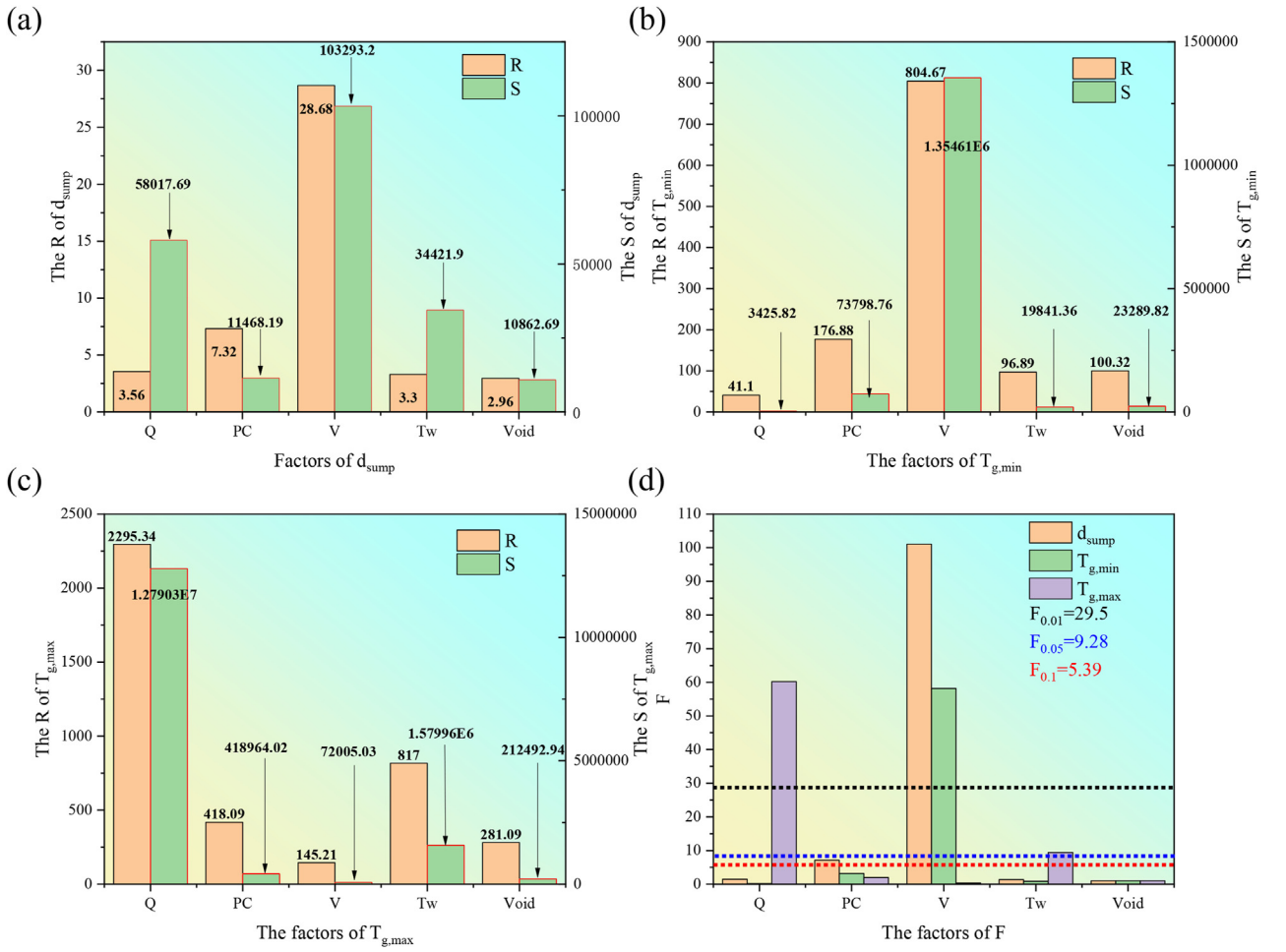


**Fig. 16 – The R, S and F of factors corresponding to index: (a) range and variance of $d_{smup}$; (b) range and variance of $T_{g,min}$; (c) range and variance of $T_{g,max}$; (d) significance of $d_{smup}$, $T_{g,min}$ and $T_{g,max}$.**

$$q_c = C_{p,w} k_w \left(\frac{\rho_w g}{\mu_w}\right)^{0.33} \left(\frac{1.6\rho_w \dot{Q}}{\mu_w}\right)^{0.84} \left(\frac{c_{p,w}\mu_w}{k_w}\right)^{0.74} (T_s - T_w) \quad (36)$$

In consequence, the thermal condition of B5 and B7 can be classified into two parts: the impingement zone and free-falling zone. The value of $C_{p,w}$, $k_w$, $\rho_w$ and $\mu_w$ can be obtained from Table 5. Similarly, the qnb is obtained from (Fig. 13 (a)), as can be seen, the $\ln(q_{nb})$ exhibits a linear relationship with $\ln(T_s - T_{sat})$ with an expression seen in Eq (37) as follows:

$$ln\ q_{nb} = 0.83\ ln(T_s - T_{sat}) + 8.11292, R^2 = 0.92 \quad (37)$$

Based on Eq 22–26 and Eq (36), the total heat flux density $q_{total}$ at impingement zone can be expressed in Eq (38):

$$q_{total} = q_{nb} + q_c = 22616.58(T_s - T_w)(\dot{Q})^{0.84} + 3327.58(T_s - T_{sat})^{0.83} \quad (38)$$

The total heat flux density at free-falling zone are shown in Table 8, and the detailed information are seen in Eq 39 and 40. As mentioned above, the $q_{nb}$ and $q_c$ are obtained by (Fig. 13 (a)) and (Fig. 13 (b)) respectively. The detail of $q_{fb}$ can be seen in Eq (14) of section 3.2.

$$q_{nb} = 3327.58(T - T_{sat})^{0.83} \quad (39)$$

$$q_c = 22616.58(T_s - T_w)(\dot{Q})^{0.84} \quad (40)$$

### 3.5.4. *Bottom block zone*

At the initial process of DC casting, the melting poured on the bottom block, similar to the process of primary cooling, the rate of heat transfer between the melting and bottom block are higher due to the contact between the liquid metal and bottom block surface than the one in subsequent process because the small gap was generated by solidification. The gap between solidifying metal and bottom block will grow up with relatively low speed before the cooling water from the secondary cooling zone driven by gravity was spilled. Subsequently, the ingot base begins to deform upward with different degree which is positively correlated to rate of heat transfer, in response to the rapid thermal contraction of the sides, the four corners of ingot base have the relatively large displacements with a few tens of millimeters. This process enhances the rate of interface heat transport known as butt curl [73–78], refer to Fig. 14.

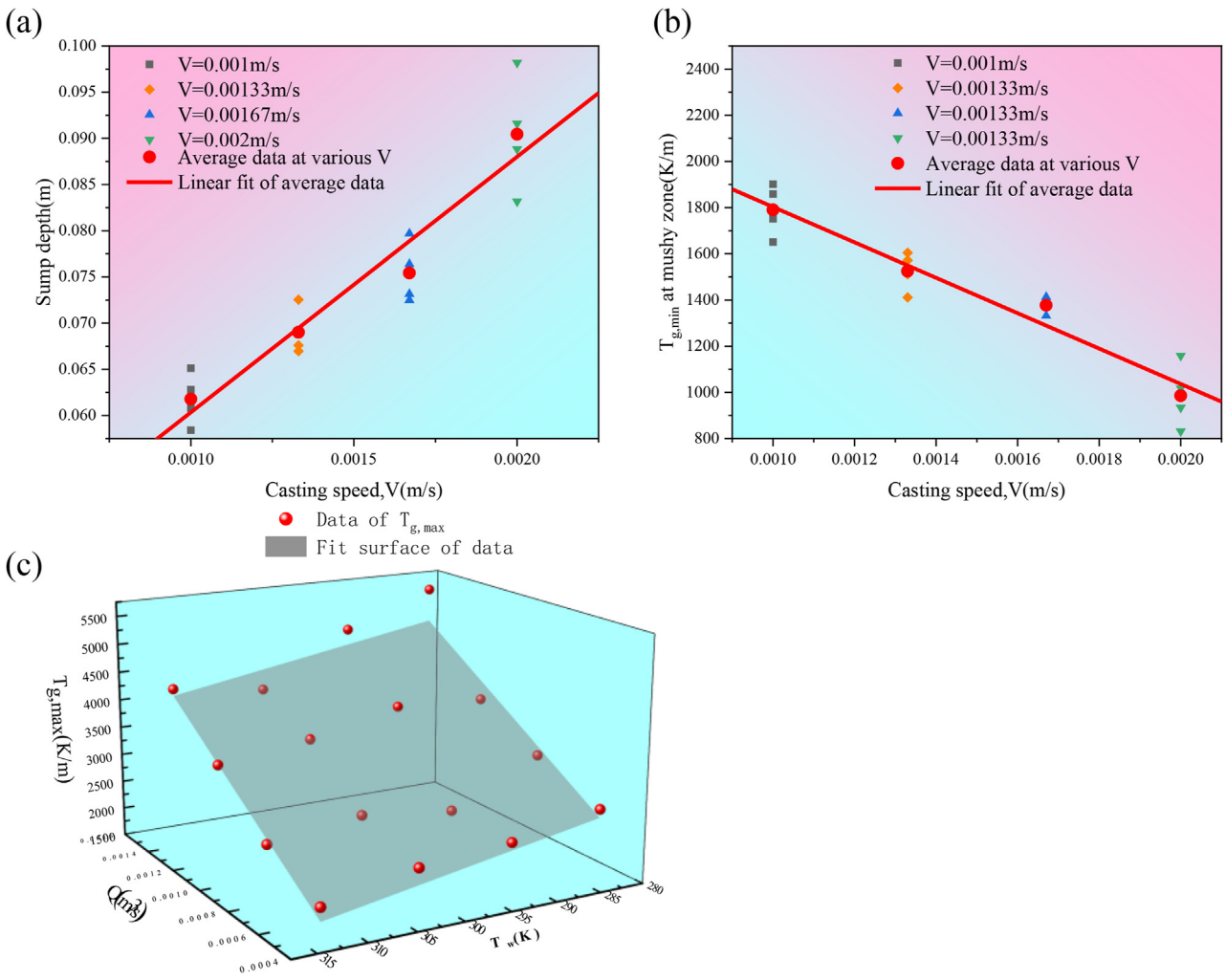


**Fig. 17 – The relationship between factors and index: (a) casting speed vs. sump depth; (b) casting speed vs. minimum of temperature gradient at mushy zone; (c) secondary cooling water flow rate and temperature of cooling water vs. maximum of temperature gradient at mushy zone.**

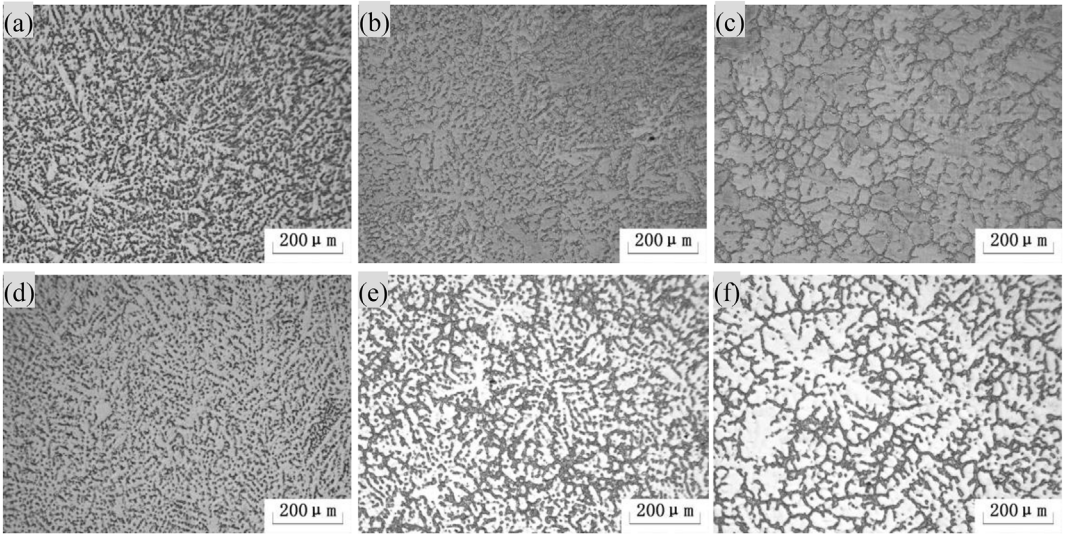


**Fig. 18 – The as-cast microstructure on width direction with different casting speed: (a–c) microstructure from pouring center to edge with 80 mm/min; (d–f) microstructure from pouring center to edge with 120 mm/min.**

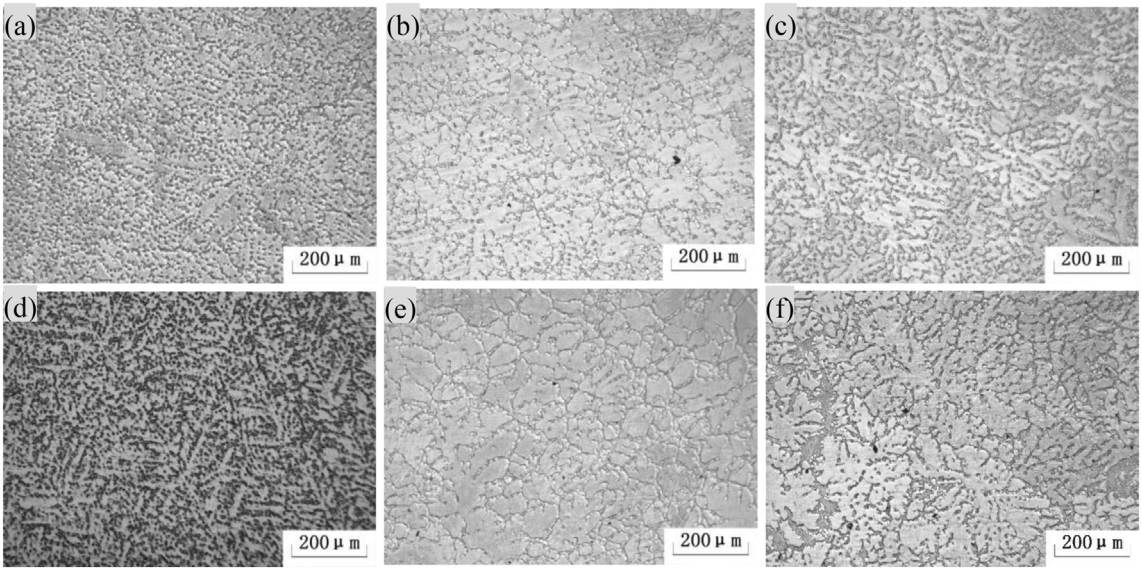


**Fig. 19 – The as-cast microstructure on thickness direction with different casting speed: (a–c) microstructure from pouring center to edge with 80 mm/min; (d–f) microstructure from pouring center to edge with 120 mm/min.**

Generally speaking, some assumptions and simplifications should be provided in numerical simulation. The vertical displacement of the base of the ingot was assumed to obey a parabolic relationship with distance and to also vary with time. The largest displacement was assumed to occur at the edges of the ingot, and no displacement was assumed to occur at the center part, as seen in Fig. 14. Moreover, the cooling water was assumed to wet the butt curl, which means there are none interaction between water and ingot at center part. The heat transfer at wetted part $q_{water}$ was simplified to match the heat transfer at free-falling zone, as seen in Table 8.

Based on the assumptions and simplification above, according to Fig. 14, the heat transfer associated with the base cooling to the bottom block has been characterized for both center parts as seen in Eq (41) and Eq (42):

$$q_{contact} = h_{contact}\left(T_{s,ingot} - T_{s,bottom\ block}\right) \tag{41}$$

$$h_{contact} = \begin{cases} 1500, T_s \geq 879 \\ 17.05\,(T_s - 791), 791 < T_s < 879 \\ 75, T_s < 791 \end{cases} \tag{42}$$

## 4. Comparison and validation

To further validate the accuracy of the secondary cooling model proposed in this paper, a comprehensive comparison is

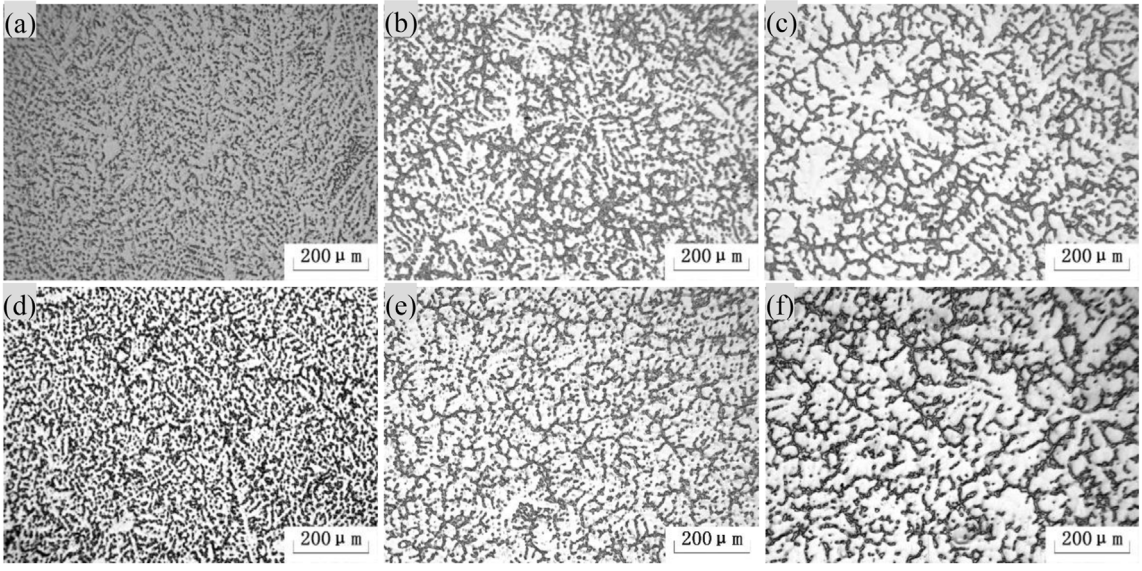


**Fig. 20 – The as-cast microstructure on width direction with different secondary cooling water flow rate: (a–c) microstructure from pouring center to edge with 40 L/min; (d–f) microstructure from pouring center to edge with 70 L/min.**

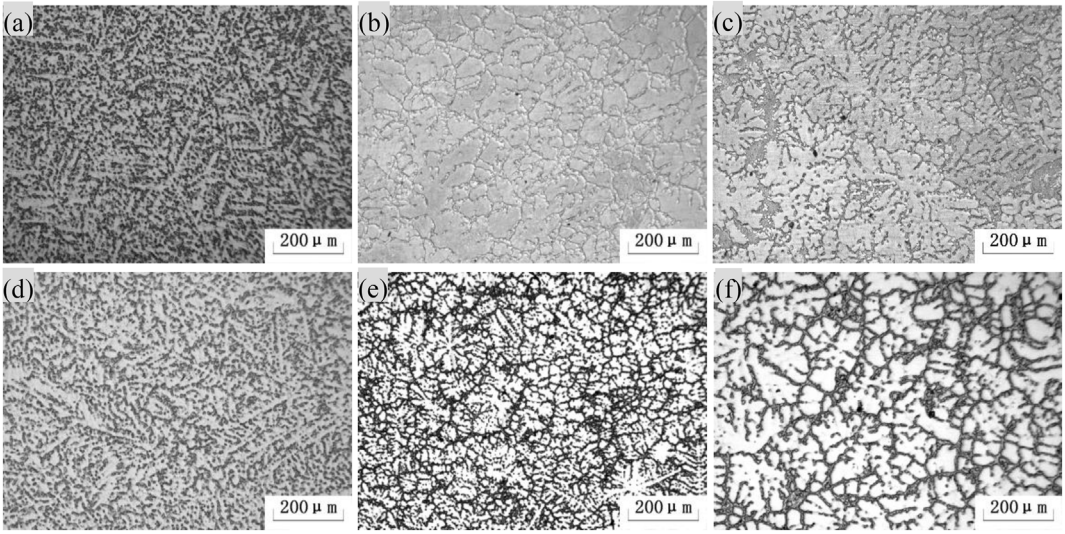


**Fig. 21 – The as-cast microstructure on thickness direction with different secondary cooling water flow rate: (a–c) microstructure from pouring center to edge with 40 L/min; (d–f) microstructure from pouring center to edge with 70 L/min.**

performed between the in-situ temperature data obtained from thermocouples in section 2.1 and the corresponding temperature data calculated based on the thermal conditions discussed earlier. This comparative analysis is presented in Fig. 15.

In the figure, the solidus line and liquidus line, which are determined through numerical simulations using the secondary cooling models, are depicted as black lines representing the width and thickness directions, respectively. Remarkably, these lines fall within the gray dotted line zone and purple dotted line zone, indicating a close agreement between the secondary cooling thermal conditions predicted by the semi-empirical models proposed in this study and the actual temperature measurements.

By comparing the calculated temperature data with the in-situ measurements, it becomes evident that the proposed secondary cooling model reliably captures the temperature distribution throughout the cooling process. This validation not only substantiates the accuracy of the thermal conditions derived from the semi-empirical models but also reinforces the overall credibility and effectiveness of the secondary cooling model put forth in this paper.

## 5. Result and discussion

Here are the results of sump depth ($d_{smup}$), minimum of temperature gradient at mushy zone ($T_{g,min}$), maximum of temperature gradient at mushy zone ($T_{g,max}$) designed by orthogonal test, calculated by numerical simulation, shown in Table 9. Combined with Fig. 21 and Fig. 22, the majority of $T_{g,max}$ located at $L_{p,e}$, which near the center of below inlet of pouring and edge as can be seen marked in gray zone in Fig. 24. Similarly, the majority of $T_{g,min}$ located at $L_p$, which is below the inlet of pouring as can be seen marked in green zone in Fig. 24.

The analysis of range $R$, sum of squared deviations $S$ and significance $F$ can be seen in Fig. 16. The $d_{smup}$ is dominated by $V$ among the factors due to the high performance of $R$ and $S$. Generally speaking, the factor is significant among others under the condition the value of $F$ is greater than $F_{0.05}$ [54–57]. The $F_{0.05}$ of multi-factors $L_{16}(4^5)$ orthogonal is 9.38. In consequence, the relationship between the $V$ and $d_{smup}$ could be established based on (Fig. 17(a)) with the value of linear correlation coefficient $R^2$ is 0.98, as follows:

$$d_{sump} = 0.033 + 27.74V, R^2 = 0.98 \tag{43}$$

Similarly, the $V$ also dominate the minimum of temperature $T_{g,min}$ at mushy zone among other factors, the relationship between $V$ and $T_{g,min}$ is provided according to (Fig. 17(b)), based on the $R$, $S$ and $F$ seen in (Fig. 16(b)), as follows:

$$T_{g,min} = 2569.15 - 766342.20V, R^2 = 0.97 \tag{44}$$

A lot of typical as-cast dendrite structure with fully developed primary dendrite and secondary dendrite are seen in Fig. 18. The average secondary dendrite arm spacing (SDAS) of the $L_p$ part with the $V$ at 80 mm/min and 120 mm/min are 11.1 μm and 13 μm respectively. The primary dendrite length increased with the increasing $V$ as seen in (Fig. 18(c)) and (Fig. 18(e)), the average of SDAS are 12 μm and 13.6 μm corresponding to the $V$ at 80 mm/min and 120 mm/min. The degeneration occurs at the edge part and the primary and secondary dendrite became shorter and thicker at relative low speed. Further, a lot of rosette crystals are seen in (Fig. 18(a)) and (Fig. 18(d)), the average of SDAS is 22.7 μm at relative high $V$. In general, the SDAS increased from the $L_p$ to edge and the value with the 80 mm/min is smaller than the $V$ at 120 mm/min especially at $L_p$ part, according to Eq (44), which means the cooling speed $V_c$ (or temperature gradient) of $L_p$ part is higher at relative lower $V$ according to Eq (45) [79–81]:

$$DAS = \beta V_c^{-\frac{1}{3}} \tag{45}$$

Where the DAS is dendrite arm spacing, β is a coefficient which relate to alloy composition and cooling condition, $V_c$ represents the cooling speed.

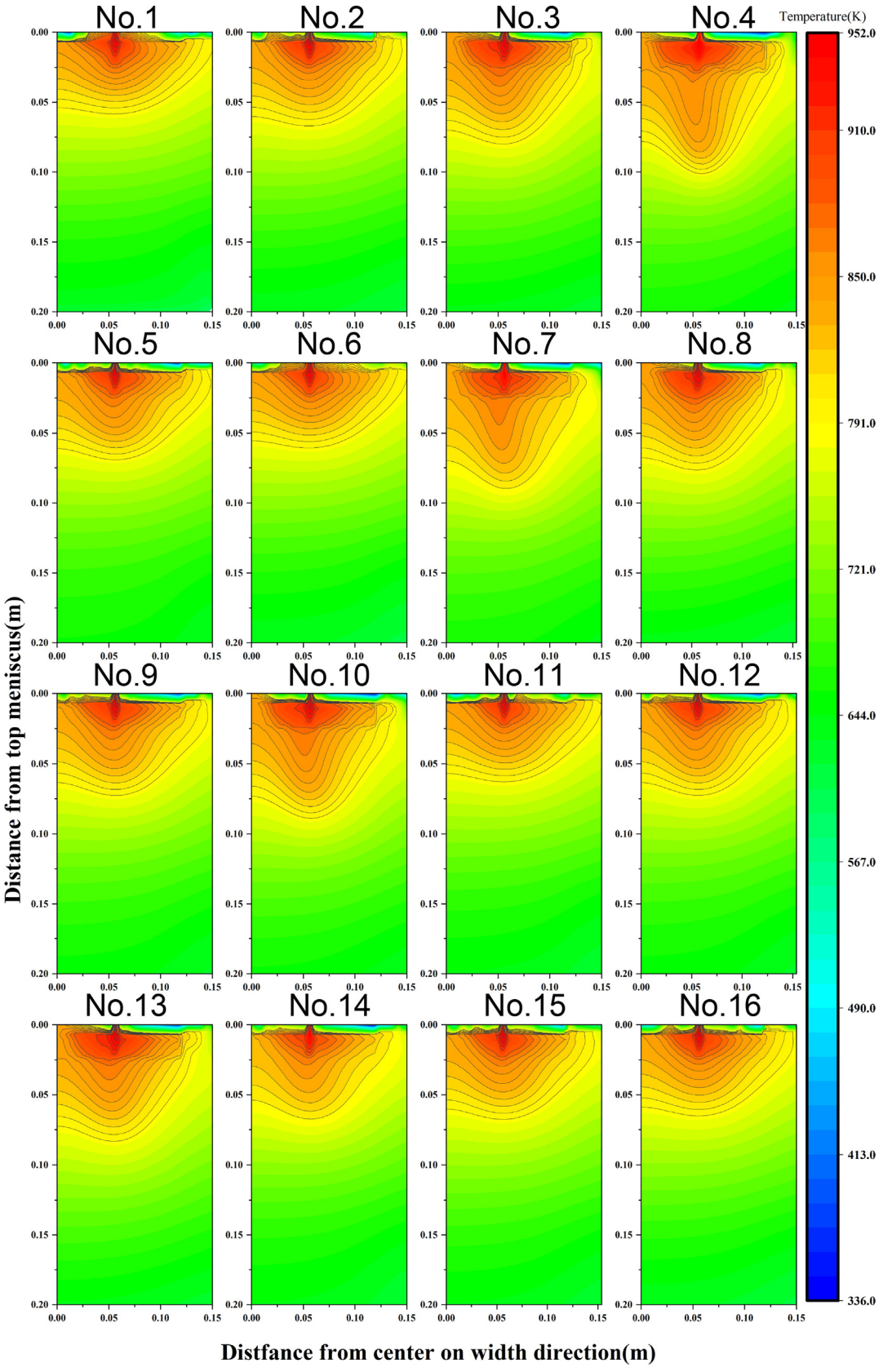


**Fig. 22 – Temperature field on width direction of symmetrical surface from No.1 to No.16.**

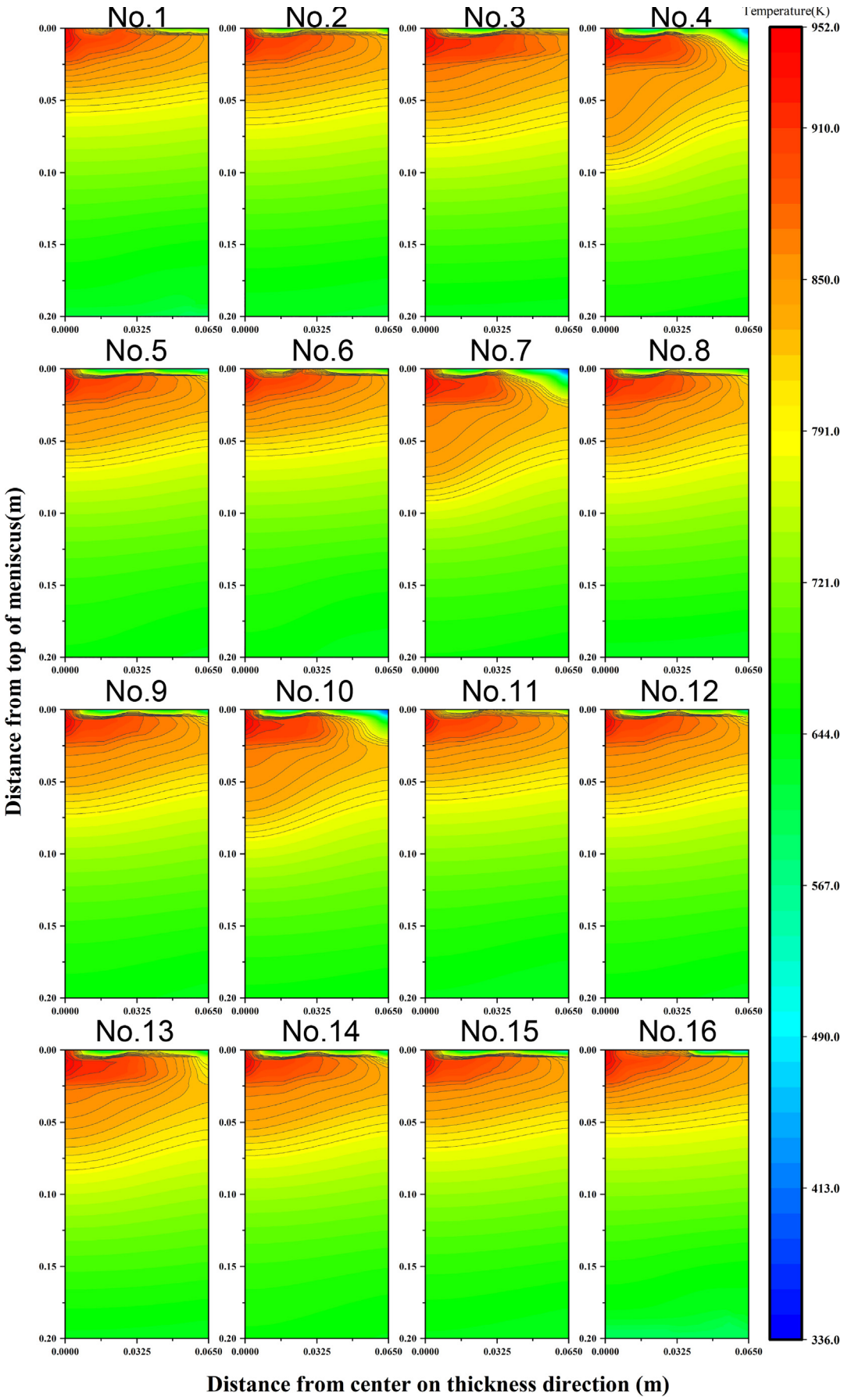


**Fig. 23 – Temperature field on thickness direction of symmetrical surface from No.1 to No.16.**

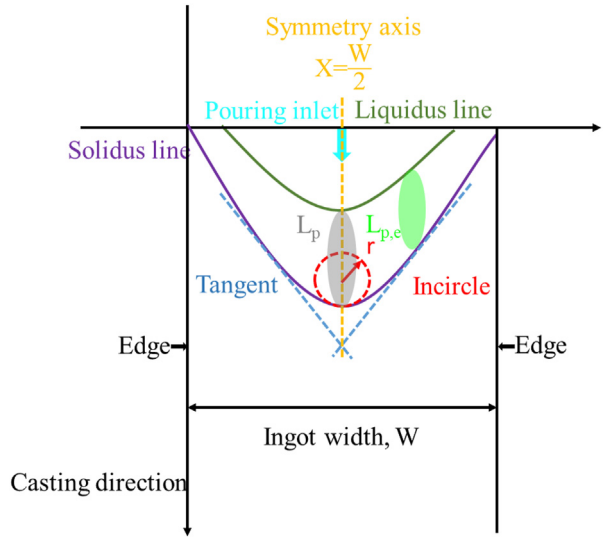


**Fig. 24 – Schematic illustration of flat parameter and steep parameter on width direction.**

Likewise, the temperature gradient $T_{g,min}$ (or cooling speed) increased from $L_p$ to edge and the similar changing law are seen in Fig. 19. In consequence, the qualitative analysis above matched the quantitative analysis as seen in Eq (44)

According to the (Fig. 16(d)) and (Fig. 17(c)), the significance of maximum of temperature gradient ($T_{g,max}$) at mushy zone revealing the influencing factor Q and $T_w$ play an important role on affecting the $T_{g,max}$, the expression is shown as follows:

$$T_{g,max} = 9195.12 + 2344770Q - 27.83T_w, R^2 = 0.87 \quad (46a)$$

The microstructure of sample with the value of cooling water flow rate 40 L/min and 70 L/min respectively are shown in Fig. 20. From the microstructure, the dendrites gradually degrade from the $L_p$ to the edge. Under two different Q, the structure is refined to a certain extent after increasing the Q. The $L_p$ part presents a typical multi-dendrite structure. After increasing the Q, the structure is refined and the secondary dendrite arm spacing is small, about 11.7 μm (Fig. 20(c)). At the $L_{p,e}$ position, it is composed of rose crystals and a small number of degraded dendrites. After increasing the water volume, the degree of dendrite degradation is more obvious, and the degree of fragmentation increases. The average secondary dendrite arm spacing is about 12.6 μm (Fig. 20(d)). The dendrites at the edge are more degraded, and the primary and secondary dendrites are obviously short and thick. The roundness of the dendrites increases, and petal-shaped crystals appear in the structure of (Fig. 20(e)). In a semi-continuous casting process, greater Q leads to greater cooling intensity. When the ingot solidifies at its edge position, it is mainly affected by primary cooling so that there is little difference in structure. As casting progresses, temperature at the edge gradually decreases. When $L_{p,e}$ position and $L_p$ begin to enter liquid phase line, under large water conditions, there is a degree of expansion of temperature difference with already solidified parts and temperature gradient is larger with faster cooling rate resulting the smaller SDAS.

**Table 10 – *B* and *K* of solidus line based on orthogonal test by numerical simulation.**

| No. | $B_w$ | $K_w$ | $B_t$ | $K_t$ |
|---|---|---|---|---|
| 1 | 1.918916203 | 4.510979 | 3.482163 | 4.222839 |
| 2 | 1.193176902 | 3.90201 | 5.57421 | 4.816813 |
| 3 | 0.836495713 | 3.318115 | 1.512306 | 2.718298 |
| 4 | 0.470050227 | 3.856547 | 2.207978 | 1.543761 |
| 5 | 1.368195753 | 3.814734 | 7.819952 | 8.51332 |
| 6 | 1.549900101 | 4.89534 | 3.968617 | 4.922839 |
| 7 | 0.632555282 | 5.892715 | 0.588677 | 6.297792 |
| 8 | 0.881118791 | 5.876754 | 2.742883 | 4.768002 |
| 9 | 1.181526442 | 4.968948 | 4.692622 | 7.094964 |
| 10 | 0.599219527 | 5.683885 | 1.021431 | 9.245919 |
| 11 | 1.400272892 | 5.862107 | 4.875037 | 5.976139 |
| 12 | 1.19588329 | 6.813461 | 4.692622 | 8.148292 |
| 13 | 0.65143325 | 6.305566 | 3.202937 | 6.192557 |
| 14 | 1.163946685 | 6.614496 | 3.461919 | 11.96997 |
| 15 | 1.168738545 | 5.923671 | 2.841718 | 7.586942 |
| 16 | 1.427174814 | 6.531236 | 2.705636 | 9.34623 |

In a semi-continuous casting process, greater secondary cooling water volume leads to greater cooling intensity. When the ingot solidifies at its edge position, there is little difference in structure. As casting progresses, temperature at the edge gradually decreases. When $L_{p,e}$ position and $L_p$ begin to enter liquid phase line, under large water conditions, there is a small degree of expansion of temperature difference with already solidified parts and temperature gradient is large with fast cooling rate. Secondary dendrite arm spacing is small.

Similarly, Fig. 21 shows the longitudinal section of the microstructure of AZ80 magnesium alloy semi-continuous casting ingot from the $L_p$ to the edge in the thickness direction under different Q. The dendrites degrade from the $L_p$ to the edge. The structure is refined and the SDAS is smaller after increasing the Q. At the $L_{p,e}$ position, it is composed of rose crystals and degraded dendrites. The dendrites at the edge are more degraded and shorter. Petal-shaped crystals appear in the structure. Compared with the width direction, the size in the thickness direction is smaller and Q can act on the $L_{p,e}$ position, obviously. Therefore, the qualitative analysis above matched the quantitative analysis as seen in Eq (46).

The analysis of the temperature field of the symmetry plane is of great significance. By analyzing the temperature field of the symmetry plane, the overall condition of the liquid cavity and paste zone can be clearly understood. The temperature distribution on both sides of the symmetry plane is symmetrical, which can reflect the overall temperature distribution of the casting process. Therefore, by analyzing the temperature field of the symmetry plane, more comprehensive information about the casting process could be gained. Here are the temperature field results at symmetrical surface designed by orthogonal test shown in Figs. 22 and 23, the temperature of mushy zone is marked with black line at the value of 791 K, 800 K, 810 K, 820 K, 830 K, 840 K, 850 K, 860 K, 870 K, 879 K respectively. As mentioned above, the $T_{g,min}$ and $T_{g,max}$ on the horizontal and vertical symmetry planes are located at the $L_p$ and $L_{p,e}$. The temperature data corresponding to space can be obtained from the above temperature field diagram.

In order to study the influence of various casting parameters on the shape of liquidus cave, flat parameters (*B*) and

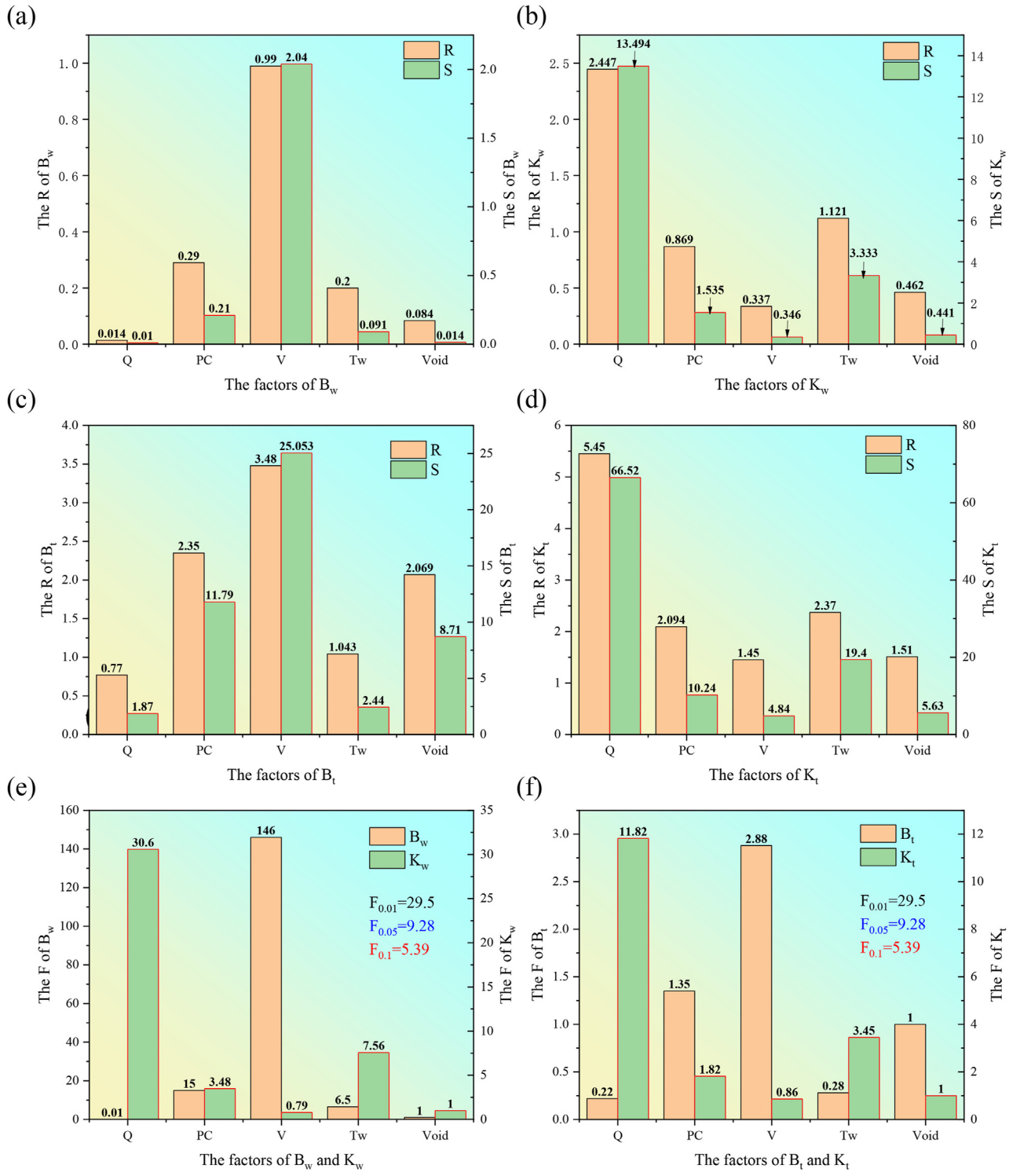


**Fig. 25 – The R, S and F of factors corresponding to index: (a) range and variance of $B_w$; (b) range and variance of $K_w$; (c) range and variance of $B_t$; (d) range and variance of $K_t$; (e) significance of $B_w$ and $K_w$; (f) significance of $B_t$ and $K_t$.**

steep parameters ($K$) are introduced to quantitatively analyze the shape of solidus lines using analytical geometry knowledge shown in Fig. 24 and Eq (46) and Eq (47) under the assumption that each solidus line is continuous function. As the value of $B$ increases, the $K$ value approaches 1, resulting in a flatter shape of the solidus line. In contrast, the solidus line becomes steeper in shape. The $B$ and $K$ on width direction ($B_w$, $K_w$) and on thickness direction ($B_t$, $K_t$) at the solidus line below

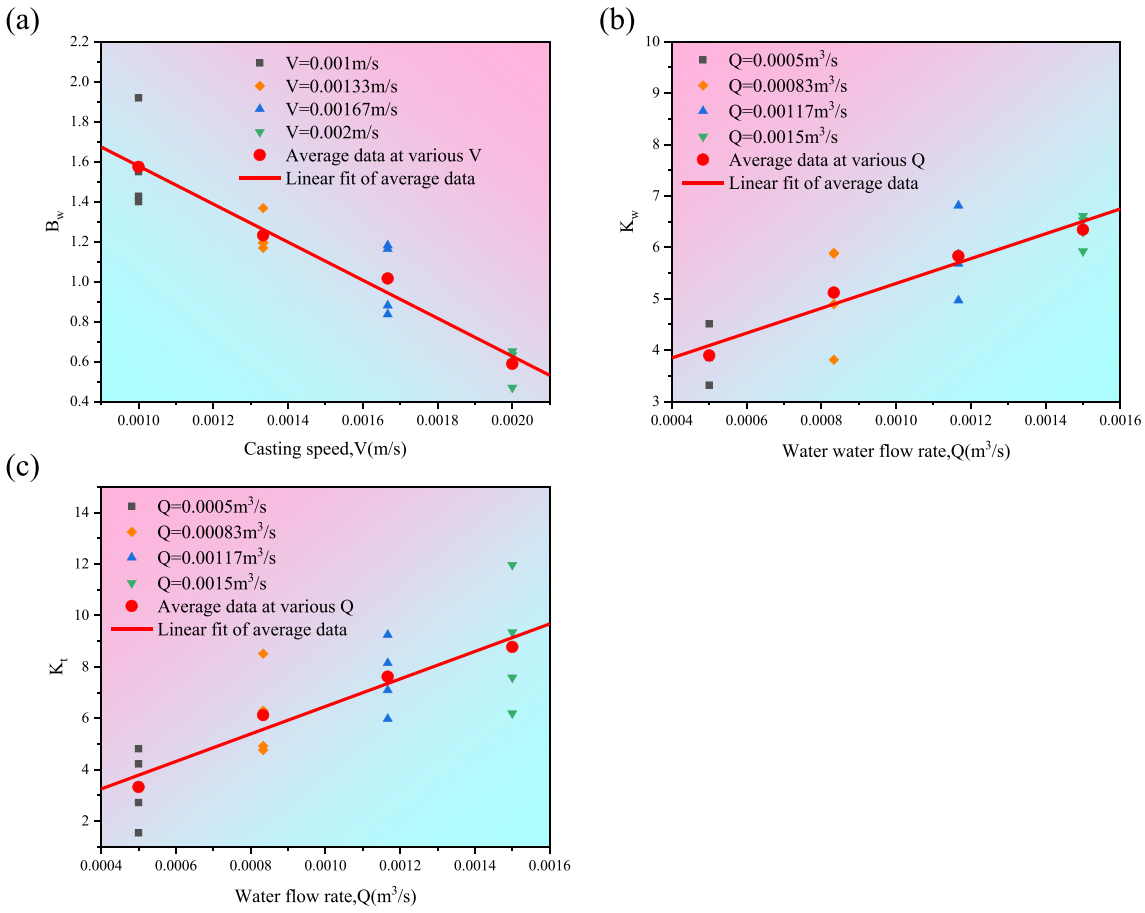


**Fig. 26 – The relationship between factors and index: (a) casting speed vs. flat parameter of solidus line on width direction; (b) secondary cooling water flow rate vs. steep parameter of solidus line on width direction; (c) secondary cooling water flow rate vs. steep parameter of solidus line on thickness direction.**

$L_p$ and the $K$ at $L_{p,e}$ of the solidus line is provided by the following Table 10. In addition, the W should be instead by T (the thickness of ingot) on thickness direction.

$$B = \frac{\left(1 + f'\left(\frac{W}{2}\right)^2\right)^{\frac{3}{2}}}{f\left(\frac{W}{2}\right) \bullet \left|f''\left(\frac{W}{2}\right)\right|} \tag{46b}$$

$$K = \frac{\frac{W}{4}f'\left(\frac{W}{4}\right) + f\left(\frac{W}{4}\right)}{f\left(\frac{W}{2}\right)} \tag{47}$$

The analysis of R, S and F shown reveals the $B_w$ is dominated by V among the factors due to the high performance of R and S as seen in Fig. 25. Generally speaking, the factor is significant among others under the condition the value of F is greater than $F_{0.05}$. The $F_{0.05}$ of multi-factors $L_{16}(4^5)$ orthogonal is 9.38. In consequence, the relationship between the V and $B_w$ could be established based on Fig with the value of linear correlation coefficient $R^2$ is 0.98, as follows Eq (48):

$$B_w = 2.53 - 951.59V, R^2 = 0.98 \tag{48}$$

Similarly, the Q dominate the $K_w$ and $K_t$ at solidus line among other factors, the relationship between Q and $K_w$, Q and $K_t$ are provided according to Fig. 26, based on the R, S and F seen in Fig. 25, as follows Eq (49) and Eq (50):

$$K_w = 2.88 + 2415.81Q, R^2 = 0.97 \tag{49}$$

$$K_t = 1.11 + 5350.90Q, R^2 = 0.97 \tag{50}$$

According to the R, S and F analysis, the F value of $B_t$ is 7.56, which is less than the $F_{0.05}$ (9.38). Therefore, B has no strong relationship with other influencing factors.

Furthermore, through the R, S and F analysis in Fig. 25, it can be seen that the change of primary cooling process conditions has an insignificant effect on the various indexes. The proportion of heat exchange during the whole semi-continuous casting process is much lower than the secondary cooling zone. Therefore, the influence of primary cooling on various casting indexes is not significant.

## 6. Conclusion

In this paper, a systematic study on heat transfer of secondary cooling has been conducted including analyzing flow boiling

mechanism of impingement zone and free-falling zone, developing the semi-empirical model of secondary cooling based on in-situ temperature measurement method and falling water film quenching test.

The main boiling mechanism at impingement zone is nucleate boiling with flow, which is not influenced by temperature variations, observed by the falling quenching test. At free-falling zone, the boiling mechanism varies with temperature. When the $T_s$ is lower than $T_{onb}$, none boiling phenomenon occurred on metal surface, and convection takes precedence. When the $T_s$ ranges between $T_{onb}$ and $T_{chf}$, nucleate boiling with flow at the solid-liquid interface becomes the dominant mechanism. Once the surface temperature reaches $T_{chf}$, a film boiling phenomenon begins to develop on the metal surface. With increasing temperature, the proportion of film boiling progressively increases, while the contribution of nucleate boiling with flow diminishes. When the surface temperature surpasses $T_{leid}$, nucleate boiling ceases, and film boiling takes over as the predominant mechanism.

The secondary cooling thermal conditions based on the semi-empirical models in this paper exhibits high accuracy by comparing the calculated data with the data gained from in-situ measurement of DC casting process.

Further, the effect and dominance of multi-parameters such as water flow rate of secondary cooling (Q), casting speed (V), the status of primary cooling zone (PC), temperature of water ($T_w$)at secondary cooling zone on the index of DC casting has been conducted by orthogonal method based on the verified thermo models.

The casting speed V dominate the casting indexes including minimum of temperature gradient $T_{g,min}$, the sump depth $d_{sump}$ and flat parameter of liquidus cave on width direction $B_w$. Similarly, the water flow rate Q dominate the casting indexes including maximum of temperature gradient $T_{g,max}$, steep parameters of liquidus cave on width $K_w$ and thickness direction $K_t$.

The detailed conclusions are presented based on the results as follows:

1) The $H_{ip}$ exhibits linear positive correlation with Q and V. The $T_i$ has limited impact on the $H_{ip}$. The expression of $H_{ip}$ is presented as follows:

$$H_{ip} = 1.08865Q^{`} + 0.06272V - 4.75597, R^2 = 0.95$$

2) The influence of the $T_i$ and Q on $T_{onb}$ is minimal. The $T_{leid}$ demonstrates a direct and proportional relationship with the $\sqrt{Q^{`}}$. These findings provide compelling evidence for a linear positive correlation between $T_{leid}$ and the $\sqrt{Q^{`}}$ and similar to $T_{chf}$:

$$T_{leid,average} = 29.06\sqrt{Q^{`}} + 526.81$$

$$T_{chf,average} = 15.90\sqrt{Q^{`}} + 561.99$$

3) Based on the opinion that flow boiling, nucleate boiling and convective heat transfer occur simultaneously. An expression for the nucleate boiling and convective heat flux density can be derived through in-situ temperature measurements during DC casting process:

$$q_{total} = q_{nb} + q_c = 22616.58(T_s - T_f)(Q^{`})^{0.84} + 3327.58(T_s - T_{sat})^{0.83}$$

4) Through the comparison of microstructures under different V (80 mm/min and 120 mm/min), the lower regions of the pouring position are more sensitive to V. This observation aligns with the fact that numerical simulations often show the $T_{g,min}$ located beneath the pouring region. Combining the R, S and F analysis of the orthogonal experimental table, the V plays a dominant role in determining the $T_{g,min}$ and $B_w$. In the numerical simulation results, V exhibit linear negative correlation with the $T_{g,min}$, $d_{sump}$ and $B_w$, as expressed below:

$$T_{g,min} = 2569.15 - 766342.20V, R^2 = 0.97$$

$$d_{sump} = 0.033 + 27.74V, R^2 = 0.98$$

$$B_w = 2.53 - 951.59V, R^2 = 0.98$$

5) By comparing the microstructures under different Q, it is evident that larger Q result in smaller average SDAS. Remarkably, this observation matches the majority result of numerical simulations. Moreover, considering the R, S and F analysis of the orthogonal experimental table, the Q plays an important role in determining $T_{g,max}$. Similarly, the relationship of $K_w$ and $K_t$ with Q also can be expressed as follows:

$$T_{g,max} = 9195.12 + 2344770Q - 27.83T_w, R^2 = 0.87$$

$$K_w = 2.88 + 2415.81Q, R^2 = 0.97$$

$$K_t = 1.11 + 5350.90Q, R^2 = 0.97$$

## Declaration of competing interest

The authors declare that they have no known competing financial interests or personal relationships that could have appeared to influence the work reported in this paper.

## Acknowledgments

This work was supported by the National Natural Science Foundation of China (51974082, 52274377); the Fundamental Research Funds for the Central Universities (Grant number: N2202018); and the Programme of Introducing Talents of

Discipline Innovation to Universities 2.0 (the 111 Project 2.0 of China, No. BP0719037).

## REFERENCES


[1] Xu T, Yang Y, Peng X, Song J, Pan F. Overview of advancement and development trend on magnesium alloy. J Magnesium Alloys 2019;7(3):536–44.
[2] Yang Y, Xiong X, Chen J, Peng X, Chen D, Pan F. Research advances in magnesium and magnesium alloys worldwide in 2020. J Magnesium Alloys 2021;9(3):705–47.
[3] Easton M, Beer A, Barnett M, Davies C, Dunlop G, Durandet Y, et al. Magnesium alloy applications in automotive structures. Jom 2008;60:57–62.
[4] Song J, She J, Chen D, Pan F. Latest research advances on magnesium and magnesium alloys worldwide. J Magnesium Alloys 2020;8(1):1–41.
[5] Wang XJ, Xu DK, Wu RZ, Chen XB, Peng QM, Jin L, et al. What is going on in magnesium alloys. J Mater Sci Technol 2018;34(2):245–7.
[6] Li N, Zheng Y. Novel magnesium alloys developed for biomedical application: a review. J Mater Sci Technol 2013;29(6):489–502.
[7] Gu XN, Zheng YF. A review on magnesium alloys as biodegradable materials. Front Mater Sci China 2010;4(2):111.
[8] Duan W, Yin S, Liu W, Yang J, Zhu Q, Bao L, et al. Numerical study of flow and heat transfer behaviors during direct-chill casting of large-size magnesium alloy billet under pulsed magnetic field. Int J Numer Methods Heat Fluid Flow 2021;31(3):829–57.
[9] Jia Y, Wang H, Le Q. Transient coupling simulation of multi-physical field during pulse electromagnetic direct-chill casting of AZ80 magnesium alloy. Int J Heat Mass Tran 2019;143:118524.
[10] Le Q, Guo S, Zhao Z, Zhang X. Numerical simulation of electromagnetic DC casting of magnesium alloys. J Mater Process Technol 2007;183(2–3):194–201.
[11] Hu W, Le Q, Zhang Z, Bao L, Cui J. Numerical simulation of DC casting of AZ31 magnesium slab at different casting speeds. J Magnesium Alloys 2013;1(1):88–93.
[12] Eskin DG, Zuidema Jr J, Savran VI, Kattttgerman L. Structure formation and macrosegregation under different process conditions during DC casting. Mater Sci Eng, A 2004;384(1–2):232–44.
[13] Eskin DG, Savran VI, Katgerman L. Effects of melt temperature and casting speed on the structure and defect formation during direct-chill casting of an Al-Cu alloy. Metall Mater Trans 2005;36:1965–76.
[14] Dong J, Zhao Z, Cui J, Yu F, Ban C. Effect of low-frequency electromagnetic casting on the castability, microstructure, and tensile properties of direct-chill cast Al-Zn-Mg-Cu alloy. Metall Mater Trans 2004;35:2487–94.
[15] Du Q, Eskin DG, Katgerman L. The effect of ramping casting speed and casting temperature on temperature distribution and melt flow patterns in the sump of a DC cast billet. Mater Sci Eng, A 2005;413:144–50.
[16] Zhao Z, Cui J, Dong J, Zhang B. Effect of low-frequency magnetic field on microstructures and macrosegregation of horizontal direct chill casting 7075 aluminum alloy. J Mater Process Technol 2007;182(1–3):185–90.
[17] Suyitno, Savran VI, Katgerman L, Eskin DG. Effects of alloy composition and casting speed on structure formation and hot tearing during direct-chill casting of Al-Cu alloys. Metall Mater Trans 2004;35:3551–61.
[18] Jia Y, Hou J, Wang H, Le Q, Lan Q, Chen X, et al. Effects of an oscillation electromagnetic field on grain refinement and Al8Mn5 phase formation during direct-chill casting of AZ31B magnesium alloy. J Mater Process Technol 2020;278:116542.
[19] Baserinia AR, Ng H, Weckman DC, Wells MA, Barker S, Gallerneault M. A simple model of the mold boundary condition in direct-chill (DC) casting of aluminum alloys. Metall Mater Trans B 2012;43:887–901.
[20] Lei B, Zhang Z, Le Q, Ru L, Cui J. Heat transfer behavior of AZ80–1% Y alloy during low-frequency electromagnetic casting. Trans Nonferrous Metals Soc China 2015;25(11):3618–24.
[21] Prasad A, Bainbridge IF. Experimental determination of heat transfer within the metal/mold gap in a DC casting mold: Part II. Effect of casting metal, mold material, and other casting parameters. Metall Mater Trans 2013;44:3099–113.
[22] Prasad A, Bainbridge I. Experimental determination of heat transfer across the metal/mold gap in a direct chill (DC) casting mold—Part I: effect of gap size and mold gas type[J]. Metall Mater Trans 2013;44:456–68.
[23] Tang MO, Jun X, Zhang ZF, Bai YL. Effects of annulus gap on flow and temperature field in electromagnetic direct chill casting process. Trans Nonferrous Metals Soc China 2011;21(5):1123–9.
[24] Zhang L, Eskin DG, Miroux A, Subroto T, Katgerman L. Effect of inlet geometry on macrosegregation during the direct chill casting of 7050 alloy billets: experiments and computer modelling[C]. In: IOP ConferenceSeries: materials Science and Engineering. IOP Publishing; 2012. p. 012019. 33(1).
[25] Zhang Y, Li R, Li X, Yang Y, Chen P, Dong F, et al. Possible effects and mechanisms of ultrasonic cavitation on oxide inclusions during direct-chill casting of an Al alloy. Metals 2018;8(10):814.
[26] Xu SW, Oh-ishi K, Kamado S, Takahashi H, Homma T. Effects of different cooling rates during two casting processes on the microstructures and mechanical properties of extruded Mg–Al–Ca–Mn alloy. Mater Sci Eng, A 2012;542:71–8.
[27] Hao H, Maijer DM, Wells MA, Cockcroft SL, Sediako D, Hibbins S. Development and validation of a thermal model of the direct chill casting of AZ31 magnesium billets. Metall Mater Trans 2004;35:3843–54.
[28] Hao H, Maijer DM, Wells MA, Phillion A, Corkcroft SL. Modeling the stress-strain behavior and hot tearing during direct chill casting of an AZ31 magnesium billet. Metall Mater Trans 2010;41:2067–77.
[29] Caron E, Wells MA. Secondary cooling in the direct-chill casting of magnesium alloy AZ31. Metall Mater Trans B 2009;40:585–95.
[30] Jafari H, Idris MH, Ourdjini A, Farahany S. In situ melting and solidification assessment of AZ91D granules by computer-aided thermal analysis during investment casting process. Mater Des 2013;50:181–90.
[31] Williams AJ, Croft TN, Cross M. Modeling of ingot development during the start-up phase of direct chill casting. Metall Mater Trans B 2003;34:727–34.
[32] He Y, Javaid A, Essadiqi E, Shehata M. Numerical simulation and experimental study of the solidification of a wedge-shaped AZ31 Mg alloy casting. Can Metall Q 2009;48(2):145–55.
[33] Hibbins SG. Investigation of heat transfer in DC casting of magnesium alloys[C]//International Symposium on Light Metals 1998 Metaux Legers as held at the 37 th Annual conference of metallurgists of CIM. 1998. p. 265–80.
[34] Sengupta J, Maijer D, Wells MA, Cockcroft SL, Larouche A. Mathematical modelling of the thermomechanical behavior of a 5182 aluminum ingot during the start-up phase of the DC casting process: the role of bottom block, vol. 2001. Light metals; 2001. p. 879–85.

[35] Kuo JH, Weng RJ, Hwang WS. Effects of solid fraction on the heat transfer coefficient at the casting/mold interface for permanent mold casting of AZ91D magnesium alloy. Mater Trans 2006;47(10):2547–54.
[36] Sengupta J, Cockcroft SL, Maijer D, Wells MA, Larouche A. The effect of water ejection and water incursion on the evolution of thermal field during the start-up phase of the direct chill casting process. J Light Met 2002;2(3):137–48.
[37] Mackie D, Robson JD, Withers PJ, Turski M. Characterisation and modelling of defect formation in direct-chill cast AZ80 alloy. Mater Char 2015;104:116–23.
[38] Sengupta J, Cockcroft SL, Maijer DM, Wells MA, Larouche A. On the development of a three-dimensional transient thermal model to predict ingot cooling behavior during the start-up phase of the direct chill-casting process for an AA5182 aluminum alloy ingot. Metall Mater Trans 2004;35(3):523.
[39] Reese JM. Characterization of the flow in the molten metal sump during direct chill aluminum casting. Metall Mater Trans B 1997;28:491–9.
[40] Zuidema Jr J, Katgerman L, Opstelten IJ, Rabenberg JM. Secondary cooling in DC casting: modeling and experimental results. Light metals; 2001. p. 873–8.
[41] Sengupta J, Thomas BG, Wells MA. The use of water cooling during the continuous casting of steel and aluminum alloys. Metall Mater Trans 2005;36:187–204.
[42] Hou J, Le Q, Chen X, Hu W, Ning F, Guo R, et al. Secondary cooling analysis of AZ80Y magnesium alloy slab during DC casting by modelling and verification based on experiment. Crystals 2022;12(11):1515.
[43] Drezet JM, Rappaz M, Grün GU, Gremaud M. Determination of thermophysical properties and boundary conditions of direct chill-cast aluminum alloys using inverse methods. Metall Mater Trans 2000;31:1627–34.
[44] Sai Divya PV, Penumakala PK, Nallathambi AK. Influence of secondary cooling strategies on thermal gradients in the direct chill casting of magnesium alloys. J Therm Anal Calorimetry 2022:1–16.
[45] Bolduc S, Kiss LI. Sensitivity study of the influence of the water boiling parameters on aluminum semi-continuous DC casting. Int J Therm Sci 2020;151:106276.
[46] Caron E, Wells MA. Film boiling and water film ejection in the secondary cooling zone of the direct-chill casting process. Metall Mater Trans B 2012;43:155–62.
[47] Caron EJFR, Wells MA. Effect of advanced cooling front (ACF) phenomena on film boiling and transition boiling regimes in the secondary cooling zone during the direct-chill casting of aluminium alloys[C]//Materials science forum, vol. 519. Trans Tech Publications Ltd; 2006. p. 1687–92.
[48] Caron EJFR, Baserinia AR, Ng H, Wells MA, Weckman DC. Heat-transfer measurements in the primary cooling phase of the direct-chill casting process. Metall Mater Trans B 2012;43:1202–13.
[49] Hu W, Jia Y, Chen X, Le Q, Chen L, Chen S. Determination of secondary cooling zone heat transfer coefficient with different alloy types and roughness in DC casting by inverse heat conduction method[J]. Crystals 2022;12(11):1571.
[50] Bakken JA, Bergström T. Heat transfer measurements during DC casting of aluminium part i: measurement technique. Essential Readings in Light Metals 2016;3:646–52.
[51] Zhang J, Delichatsios MA. Determination of the convective heat transfer coefficient in three-dimensional inverse heat conduction problems. Fire Saf J 2009;44(5):681–90.
[52] Xia S, Lin R, Cui X, Shan J. The application of orthogonal test method in the parameters optimization of PEMFC under steady working condition. Int J Hydrogen Energy 2016;41(26):11380–90.
[53] Wang B, Lin R, Liu D, Xu J, Feng B. Investigation of the effect of humidity at both electrode on the performance of PEMFC using orthogonal test method. Int J Hydrogen Energy 2019;44(26):13737–43.
[54] Zheng W, Dong J, Zhang L, Chen Z. Heating performance for a hybrid radiant-convective heating terminal by orthogonal test method. J Build Eng 2021;33:101627.
[55] Yin W, Zhou G, Liu D, Meng Q, Zhang Q, Jiang T. Numerical simulation and application of entrainment dust collector for fully mechanized mining support based on orthogonal test method. Powder Technol 2021;380:553–66.
[56] Li Y, She L, Wen L, Zhang Q. Sensitivity analysis of drilling parameters in rock rotary drilling process based on orthogonal test method. Eng Geol 2020;270:105576.
[57] Chen M, Zhang Z, Deng Q, Feng Y, Wang X. Optimization of underfloor air distribution systems for data centers based on orthogonal test method: a case study. Build Environ 2023;232:110071.
[58] Bennon WD, Incropera FP. A continuum model for momentum, heat and species transport in binary solid-liquid phase change systems-I. Model formulation. Int J Heat Mass Tran 1987;30(10):2161–70.
[59] Zhang H, Nagaumi H, Cui J. Coupled modeling of electromagnetic field, fluid flow, heat transfer and solidification during low frequency electromagnetic casting of 7XXX aluminum alloys. Mater Sci Eng, A 2007;448(1–2):177–88.
[60] Köhler C, Specht E, Jeschar R. Heat transfer with film quenching of vapourizing liquids. Steel Rrsearch 1990;61(11):553–9.
[61] Liu Z, Winterton RHS. A general correlation for saturated and subcooled flow boiling in tubes and annuli, based on a nucleate pool boiling equation. Int J Heat Mass Tran 1991;34(11):2759–66.
[62] Yan J, Bi Q, Liu Z, Zhu G, Cai L. Subcooled flow boiling heat transfer of water in a circular tube under high heat fluxes and high mass fluxes. Fusion Eng Des 2015;100:406–18.
[63] Yin CP, Yan YY, Lin TF, Yang BC. Subcooled flow boiling heat transfer of R-134a and bubble characteristics in a horizontal annular duct. Int J Heat Mass Tran 2000;43(11):1885–96.
[64] Kandlikar SG. Heat transfer characteristics in partial boiling, fully developed boiling, and significant void flow regions of subcooled flow boiling. 1998.
[65] Huang S, Wang L, Pan Z, Zhou Z. Experimental investigation of a new hybrid structured surface for subcooled flow boiling heat transfer enhancement. Appl Therm Eng 2021;192:116929.
[66] Lie YM, Lin TF. Subcooled flow boiling heat transfer and associated bubble characteristics of R-134a in a narrow annular duct. Int J Heat Mass Tran 2006;49(13–14):2077–89.
[67] Sun Y, Zhang L, Xu H, Zhong X. Subcooled flow boiling heat transfer from microporous surfaces in a small channel. Int J Therm Sci 2011;50(6):881–9.
[68] Chen JC. Correlation for boiling heat transfer to saturated fluids in convective flow. Ind Eng Chem Process Des Dev 1966;5(3):322–9.
[69] Rohsenow WM, Hartnett JP, Cho YI. Handbook of heat transfer[M]. New York: Mcgraw-hill; 1998.
[70] Rohsenow WM. A method of correlating heat-transfer data for surface boiling of liquids. Trans Am Soc Mech Eng 1952;74(6):969–75.
[71] Mikic BB, Rohsenow WM. A new correlation of pool-boiling data including the effect of heating surface characteristics. 1969.

[72] Robinson AJ, Schnitzler E. An experimental investigation of free and submerged miniature liquid jet array impingement heat transfer. Exp Therm Fluid Sci 2007;32(1):1–13.
[73] Drezet JM, Rappaz M. Modeling of ingot distortions during direct chill casting of aluminum alloys. Metall Mater Trans 1996;27:3214–25.
[74] Droste W, Drezet JM, Grün GU, Schneider W. 3D-Modeling of ingot geometry development of DC-cast aluminum ingots during the start-up phase. Continuous Casting; 2000. p. 175–83.
[75] Abishek S, Narayanaswamy R, Narayanan V. Effect of heater size and Reynolds number on the partitioning of surface heat flux in subcooled jet impingement boiling. Int J Heat Mass Tran 2013;59:247–61.
[76] Ishikawa N. Numerical simulation of butt curl in the semi-DC casting of aluminum slabs, vol. 28. Furukawa Review; 2005.
[77] Grealy GP, Davis JL, Jensen EK, Tøndel PA, Moritz J. Advances for DC ingot casting: part 2—heat transfer and casting results. Essent Readings Light Met 2016;3:672–80.
[79] Luo T, Ji H, Jie CUI, Zhao FZ, Feng XH, Li YJ, et al. As-cast structure and tensile properties of AZ80 magnesium alloy DC cast with low-voltage pulsed magnetic field. Trans Nonferrous Metals Soc China 2015;25(7):2165–71.
[80] Shahzad M, Wagner L. Influence of extrusion parameters on microstructure and texture developments, and their effects on mechanical properties of the magnesium alloy AZ80. Mater Sci Eng, A 2009;506(1–2):141–7.
[81] Chen X, Jia Y, Le Q, Yu F. Understanding the influence of ultrasonic streaming on solidification of AZ80 magnesium alloy during direct-chill casting using a transient coupling modeling. J Mater Res Technol 2021;14:1154–66.

## FURTHER READING

[78] Huang Z, Qi C, Zou J, Lai H, Guo H, Wang J. Edge crack damage analysis of AZ31 magnesium alloy hot-rolled plate improved by vertical roll pre-rolling. J Magnesium Alloys 2021;11:2151–64.